



# Tuning of photoinduced resistive switching characteristics of MoS<sub>2</sub>/PVA photomemristor via ultrasonication

Krishma Anand, Ravneet Kaur, S.K. Tripathi\*

Department of Physics, Centre of Advanced Study in Physics, Panjab University, Chandigarh 160014, India



## ARTICLE INFO

### Keywords:

Hydrothermal synthesis  
Transition metal dichalcogenides (TMDs)  
Polymer nanocomposites  
Photomemristors  
Charge storage  
Hysteresis curve  
 $I_{on}/I_{off}$  ratio

## ABSTRACT

In the present study, we have used a simple, cost effective and environment friendly hydrothermal method to synthesize the few layered MoS<sub>2</sub> nanosheets (NSs). We have synthesized MoS<sub>2</sub>/PVA nanocomposites (NCPs) with four different concentrations of MoS<sub>2</sub> (0.1 wt%, 0.5 wt%, 1 wt% and 1.5 wt%) within the polymer matrix by utilizing the chemical route *In-situ* method. The structural and morphological investigations have been conducted with the help of X-ray diffraction (XRD) and Field Effect Scanning Electron Microscopy (FESEM), respectively. The UV-visible (UV-Vis) spectroscopy has been employed to study the linear absorption spectra and to calculate the band gap value using Tauc's plot method for the as synthesized few layered MoS<sub>2</sub> NSs. The calculated band gap of MoS<sub>2</sub> NSs comes out to be 1.62 eV. Photoluminescence (PL) spectroscopy has been employed to record the linear emission characteristics of MoS<sub>2</sub> NSs. High Resolution Transmission Electron Microscopy (HRTEM) have been used to calculate the particle size of synthesized MoS<sub>2</sub> NSs. We have fabricated a photomemristive device with architecture Ag/MoS<sub>2</sub>-PVA/FTO with the help of a simple and cost effective drop casting method. The influence of the concentration of MoS<sub>2</sub> as well as the ultrasonication time duration on the performance of MoS<sub>2</sub>/PVA based photomemristor have been studied. The cyclic I-V measurements show hysteresis and confirm the charge storage in the fabricated device. Further, we have studied the WRER sequence and endurance characteristics of the fabricated photomemristive device over 100 cycles. The maximum  $I_{on}/I_{off}$  value has been obtained in the case of 1 wt% concentration of MoS<sub>2</sub> within the polymer matrix with 8 h of sonication and it comes out to be  $\sim 1.68 \times 10^2$  and  $3 \times 10^2$  in the absence and presence of external light source, respectively. The fabricated device is stable and reliable as confirmed by WRER sequences and endurance characteristics.

## 1. Introduction

Recently the field of photomemristors has gained a lot of scientific attention due to their marvelous benefits like preventing data shuffling, cost-efficient, high-speed data storage and less power consumption, etc. [1]. Basically, a memristor is a non-volatile, non-linear electronic device that restricts the amount of current that can flow through a circuit and retains the amount of charge that has earlier passed through it. The most interesting feature of a memristor is that we can tune its resistance state with the alteration of an applied external bias. The device can be switched from a Low resistance state (LRS) to a high resistance state (HRS) and vice-versa. Photomemristor is a light-sensitive memristor in which switching of resistance state can be triggered or enhanced with the help of incident light photons. The photomemristors will let the optoelectronic devices come to fruition because they incorporate the positive aspects of optics and electronics in an innovative aspect [2].

Recently 2D materials have gained a lot of attention in the field of optoelectronics due to their unique, structural, optical and electrical properties. Various 2D materials such as graphene, Mxene, black phosphorous and Transition metal dichalcogenides (TMDs) have gained a lot of scientific attention in the field of optoelectronics so far. The use of graphene in the area of optoelectronics is somewhat restricted by its zero band gap. Our main emphasis is on the 2D TMDs due to their tunable optical and electrical properties. We can remould the various characteristics of TMDs by just altering their layer thickness and this feature makes them unique. We can tune their electrical properties by changing the electric field or applying external bias or doping or photo irradiation. When TMDs got transmuted from their bulk form to nanosheets (NSs) form, their optical and electrical properties got transfigured to a greater extent and that makes them suitable for outstanding photoelectronic devices. Out of all these 2D TMDs, our primary focus will be on MoS<sub>2</sub> NSs due to their eminent structural stability, mechanical flexibility, high

\* Corresponding author.

E-mail address: [surya@pu.ac.in](mailto:surya@pu.ac.in) (S.K. Tripathi).

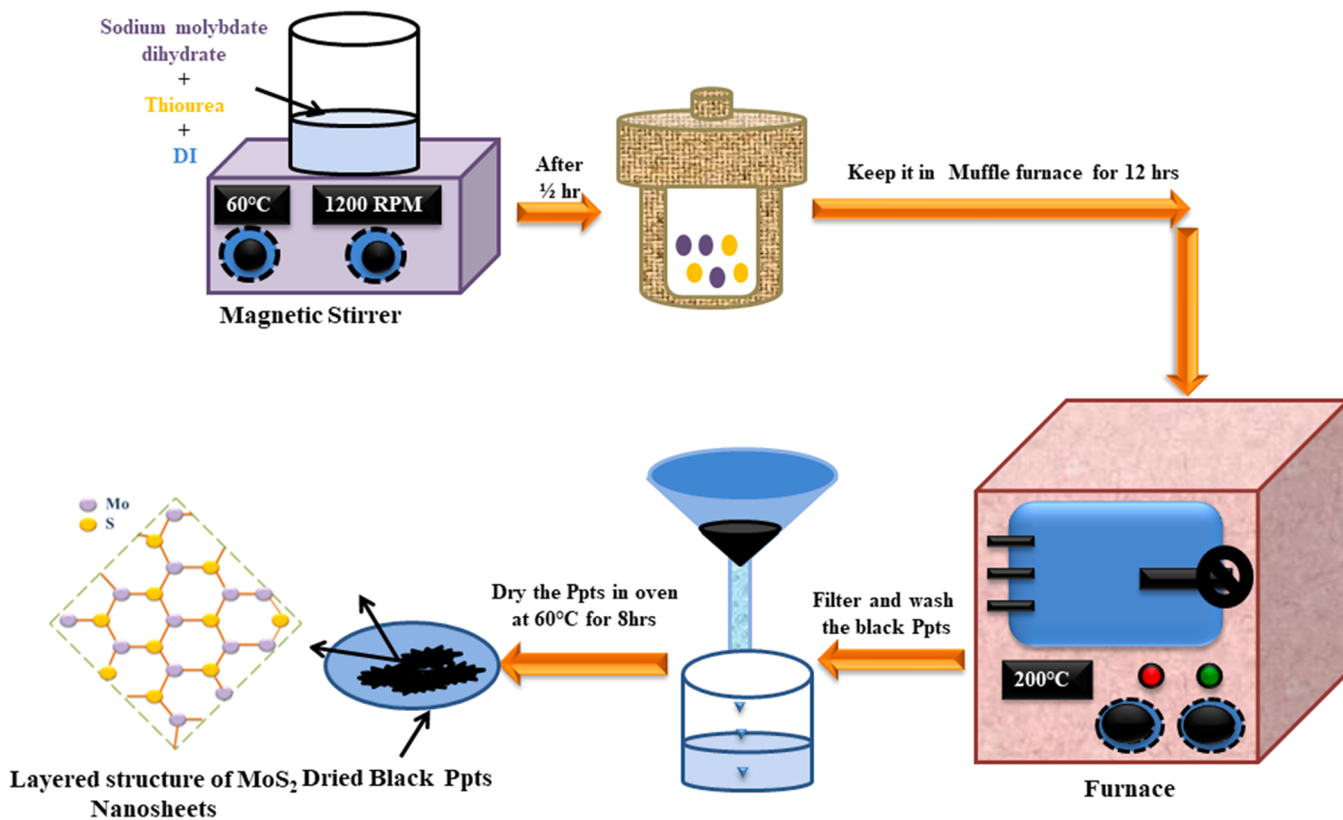


Fig. 1. Schematic of hydrothermal synthesis of few layered MoS<sub>2</sub> NSs.

carrier mobility and tunable optical properties among other TMDs [3]. The excellent electrical properties of MoS<sub>2</sub> encourage us to investigate their charge storage capabilities. Prasanna et al. [4] have grown the MoS<sub>2</sub>/CF nanostructures via hydrothermal method and further annealed to form MoS<sub>2</sub>/MoO<sub>3</sub> nanostructures. The average carrier mobility and electrical conductivity of MoS<sub>2</sub>/CF nanostructure is ~69.74 cm<sup>2</sup>/Vs and ~ 30.4 S cm<sup>-1</sup> at 373 K, respectively. Lee et al. [5] have synthesized MoS<sub>2</sub> NSs by mild grinding and delamination process and reported the electrical conductivity to be ~ 9.4 × 10<sup>-7</sup> S cm<sup>-1</sup> (at room temperature) and 2.2 × 10<sup>-4</sup> S cm<sup>-1</sup> at 373 K. Tang et al. [6] reported the electrical conductivity of raw MoS<sub>2</sub> and MoS<sub>2</sub> NSs synthesized by microwave assisted wet chemical route to be ~ 4.43 × 10<sup>-4</sup> Scm<sup>-1</sup> and 3.97 × 10<sup>-4</sup> Scm<sup>-1</sup>, respectively. Gunasekaran et al. [7] have synthesized the MoS<sub>2</sub> NSs with the help of supercritical fluid method and reported the carrier mobility of MoS<sub>2</sub> NSs to be 1530 cm<sup>2</sup>/Vs. Kim et al. [8] have synthesized the MoS<sub>2</sub> flakes from bulk MoS<sub>2</sub> single crystal via mechanical exfoliation and reported the electron mobility increased from ~10 to ~18 cm<sup>2</sup>/Vs as the number of layers increase from 1 to 6, respectively. The influence of the MoS<sub>2</sub> layer's dielectric constant and contact resistance on thickness have been concluded in paper to be the cause of the improved mobility of MoS<sub>2</sub>. Thus the enhanced carrier mobility and electrical conductivity in case of MoS<sub>2</sub> provides high I<sub>on</sub>/I<sub>off</sub> ratios, stability, charge retention and switching speed in memory device applications. Further, the absorption spectra of MoS<sub>2</sub> lie within the visible region of electromagnetic spectrum and hence make this material photo responsive and suitable for photoelectric based applications [9]. In this article, we have utilized the hydrothermal method for the synthesis of MoS<sub>2</sub> NSs. This method provides easy and precise control over the size of nanoparticles (NPs) and their morphology.

Several researchers have reported switching memory devices based upon TMDs. Liu et al. [10] have constructed the device Ti/MoS<sub>2</sub>/Pt and investigated their switching behavior within the voltage range -0.8 V to 0.8 V. They have obtained an I<sub>on</sub>/I<sub>off</sub> ratio of approximately 300. They

have further reported that the I<sub>on</sub>/I<sub>off</sub> ratio remained stable even after 10<sup>4</sup> consecutive cycles. Yin et al. [11] have observed the switching behavior of MoS<sub>2</sub>/GO nanocomposite (NCP) with architecture Al/MoS<sub>2</sub>: GO/ITO and obtained the I<sub>on</sub>/I<sub>off</sub> ratio ~10<sup>2</sup> with switching voltage < 1.5 V. Dong et al. [12] have explored the switching characteristics of MoSe<sub>2</sub> with architecture Ag/MoSe<sub>2</sub>/Cu and obtained the I<sub>on</sub>/I<sub>off</sub> ratio of the order of 10<sup>2</sup> over 10<sup>3</sup> cycles and at operating voltage < 1 V. Resistive switching device with architecture ITO/MoSe<sub>2</sub>/Ag and the I<sub>on</sub>/I<sub>off</sub> ratio > 10<sup>2</sup> over more than 100 cycles have been reported by Saini et al. [13]. Various researchers have also investigated the resistive switching devices based upon the polymer NCPs because they provide a new method to improve the processibility and stability of materials with interesting optical, mechanical and electrical properties. Dlamini et al. [14] have investigated the resistive switching behavior of PVP:MoS<sub>2</sub> NCP with device structure as Glass/Al/PVP:MoS<sub>2</sub>/Ag and obtained I<sub>on</sub>/I<sub>off</sub> ratio of the order of 10<sup>2</sup>. Deb et al. [15] have studied the switching behavior of MoS<sub>2</sub>:PEO (polyethylene oxide) within the voltage range from -4 V to 4 V and obtained the I<sub>on</sub>/I<sub>off</sub> ratio of the order of 10<sup>1</sup>. MoS<sub>2</sub>:PVA based memristive device exhibits the I<sub>on</sub>/I<sub>off</sub> ratio ~ 1.28 × 10<sup>2</sup> as reported by Rehman et al. [16]. Thus, we are motivated to create PVA/MoS<sub>2</sub> NCPs and explore their photo-enhanced resistive switching characteristics because of their remarkable qualities.

In this article, we have opted for polyvinyl alcohol (PVA) to synthesize polymer NCPs. The potential to produce extremely transparent films with good optical characteristics, high processibility, high dielectric strength, and good charge storage capacity has led to the selection of PVA as the host matrix. PVA's carbon atoms are joined to hydroxyl groups, creating a carbon chain backbone. These OH groups may contribute to the creation of polymer nanocomposite (NCP) by serving as a source of hydrogen bonding and by facilitating good dispersion. PVA is thermostable, flexible, water-soluble, and non-toxic. PVA also exhibits excellent optical properties and charge storage capacity [17, 18].

**Table 1**

Experimental condition for code name Ai, Bi, Ci, and Di; i varies from 1 to 4.

Sample Name	A1	A2	A3	A4	B1	B2	B3	B4	C1	C2	C3	C4	D1	D2	D3	D4
Concentration of MoS <sub>2</sub> NSs (wt%)	0.1	0.1	0.1	0.1	0.5	0.5	0.5	0.5	1.0	1.0	1.0	1.0	1.5	1.5	1.5	1.5
Ultrasonication Time Duration	0.5 h	4 h	8 h	12 h	0.5 h	4 h	8 h	12 h	0.5 h	4 h	8 h	12 h	0.5 h	4 h	8 h	12 h

Although MoS<sub>2</sub> and their NCP with PVA have made several individual contributions to electronic device applications, their resistive switching non-volatile memory behaviour has been rarely explored to date. To the best of our knowledge, the optically enhanced non-volatile switching behaviour of MoS<sub>2</sub>/PVA has not been studied yet. Moreover, various expensive synthesis methods such as sputtering, CVD etc. have been used to synthesize the TMDs NPs to date. In this article we have utilized the cost-effective hydrothermal method for the synthesis of few layered MoS<sub>2</sub> NSs. Further, we have utilized the chemical route *In-situ* approach to synthesize MoS<sub>2</sub>/PVA NCPs. The thin films of synthesized polymer NCPs have been deposited by cost-effective, convenient and environmental friendly drop casting method. Further, we have investigated the structural and morphological characteristics of few layered MoS<sub>2</sub> NSs and their polymer NCPs via X-ray diffraction (XRD) and Field emission scanning electron microscopy (FESEM), respectively. High resolution Transmission Electron Microscopy (HRTEM) has been studied to investigate particle size. The information regarding the trap states and defect states has been extracted from the Raman spectroscopy. Most importantly, we have investigated the non-volatile optical memristive characteristics of MoS<sub>2</sub>/PVA NCPs with varying concentration and varying sonication time durations (30 min., 4 h, 8 h and 12 h). We have obtained a maximum I<sub>on</sub>/I<sub>off</sub> ratio  $\sim 1.61 \times 10^2$  without external light source and  $\sim 3 \times 10^2$  with external light source for 1 wt% MoS<sub>2</sub>/PVA NCP with 8 hrs of sonication.

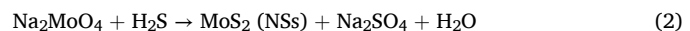
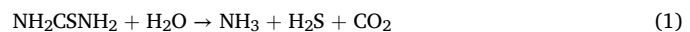
## 2. Materials and methods

### 2.1. Chemicals used

Analytical grade PVA (HIMEDIA, 99.999 %), distilled water (DI), thiourea (Sigma Aldrich, 99.999 %), and sodium molybdate dihydrate (Sigma Aldrich, 99.9 %) are utilized without additional purification.

### 2.2. Synthesis of few-layered MoS<sub>2</sub> NSs

The hydrothermal approach has been used to synthesize few-layered MoS<sub>2</sub> NSs. Thiourea and sodium molybdate are combined in a pre-determined molar ratio 1:12 and added to 60 ml DI water. For half an hour, magnetic stirring has been done at 60 °C. The mixture is placed inside a stainless steel autoclave and the autoclave is placed inside a muffle furnace at 210 °C for 12 h to conduct the hydrothermal reaction. The obtained black ppts are washed with DI water and ethanol sequentially and dried in a vacuum oven at 60 °C for 8 h. The as obtained MoS<sub>2</sub> NSs have been preserved for further use. Fig. 1 shows the schematic of the hydrothermal synthesis of MoS<sub>2</sub> NSs. The chemical reactions taking place inside the autoclave during the synthesis of few layered MoS<sub>2</sub> NSs is given by the following equations [19]



First of all, when the thiourea reacts with water molecules, there is cleavage of C-S bond due to the nucleophilic attack of water molecules and the decomposition produces S<sup>2-</sup> as represented by Eq. (1). After that the H<sub>2</sub>S formed reacts with the sodium molybdate and reduces the Mo<sup>6+</sup> to Mo<sup>4+</sup>. The Mo<sup>4+</sup> and S<sup>2-</sup> ions react to form MoS<sub>2</sub> (NSs).

### 2.3. Synthesis of MoS<sub>2</sub>/PVA nanocomposites (NCPs)

We have used an *In-situ* approach to synthesize the MoS<sub>2</sub>/PVA NCP. Initially, 0.5 wt% of PVA solution in DI has been prepared by dissolving 25 mg PVA in 5 ml DI water and stirring magnetically for 3 h at room temperature.

After that, we have synthesized 4 different concentrations (0.1 wt%, 0.5 wt%, 1 wt% and 1.5 wt%) of MoS<sub>2</sub>/PVA NCPs by using the same

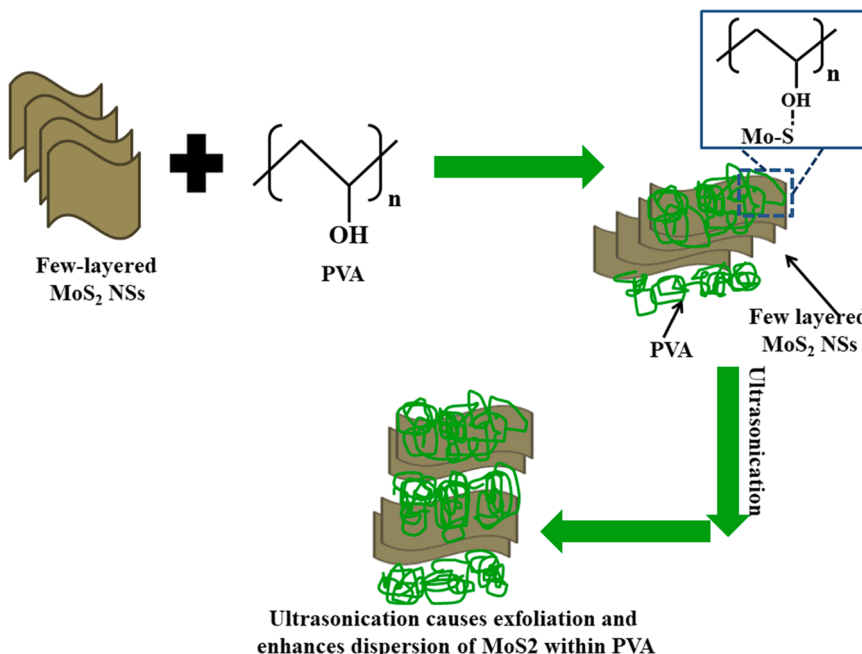


Fig. 2. Schematic illustration of linkage of MoS<sub>2</sub> with PVA and influence of ultrasonication.

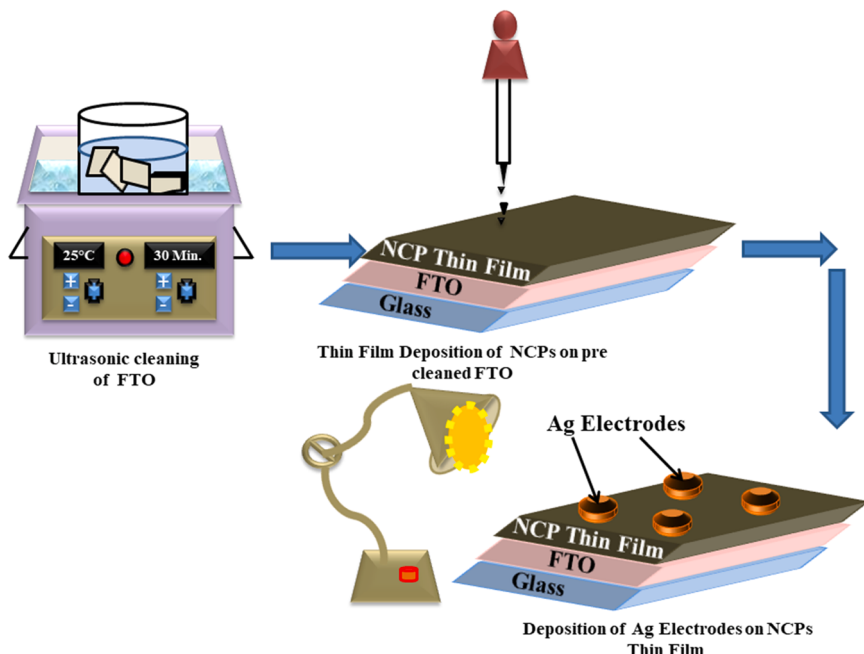


Fig. 3. Schematic of photomemristive device fabrication.

procedure as followed earlier [20]. The 0.1 wt% solution has been prepared by dissolving 5 mg of MoS<sub>2</sub> NSs in the earlier prepared 0.5 wt % PVA solution and stirring magnetically at room temperature for 6 h. We have synthesized four different samples 0.1 wt% concentration by sonicating the sample for four different time durations 30 min, 4 h, 8 h and 12 h. To synthesize the 0.5 wt%, 1 wt% and 1.5 wt% MoS<sub>2</sub>/PVA NCP, a similar procedure has been followed.

**The ultrasonication of the samples has been done to enhance the dispersivity of MoS<sub>2</sub> NSs within the PVA matrix.** The MoS<sub>2</sub> NSs got interlinked to the PVA chains as well the interlinked chains of PVA and MoS<sub>2</sub> NSs got exfoliated via ultrasonication. All the characterizations such as FESEM, RAMAN and IV shows the similar correlated results where exfoliations as well as dispersion took place. **The influence of ultrasonication time duration on the dispersion of MoS<sub>2</sub> NSs within the PVA matrix, on the exfoliation of MoS<sub>2</sub> NSs within the PVA matrix and the on the eventual properties of the composites have been further explained in FESEM scans, RAMAN spectroscopy and I-V characterization under the Section 4.5 (device characterizations) in detail later on.**

The four different samples of 0.1 wt%, 0.5 wt%, 1 wt% and 1.5 wt% are named as A1, A2, A3,A4; B1, B2, B3, B4; C1, C2, C3, C4; and D1, D2, D3, D4, respectively. Here, 0.1 wt%, 0.5 wt%, 1 wt% and 1.5 wt% of concentration are denoted by A, B, C, D and 30 min., 4h, 8 h, 12 h of sonication time durations are denoted by 1, 2, 3, 4, respectively. The experimental conditions corresponding to code name A<sub>i</sub>, B<sub>i</sub>, C<sub>i</sub>, and D<sub>i</sub>; i varies from 1 to 4, are given in Table 1 below:

The schematic illustration of linkage of MoS<sub>2</sub> NSs with polymer PVA and the influence of ultrasonication on the polymer NCP is given in Fig. 2. When MoS<sub>2</sub> NSs are added to PVA matrix, the MoS<sub>2</sub> NSs got interlinked to the polymeric chains via H-bonding. The hydroxyl (-OH) group in PVA and the electron-rich sites (-S) in MoS<sub>2</sub> NSs responsible for H-bonding. The polymer and the NSs form well-interconnected network through H-bonding. The development of stable NCPs is made possible by the H-bonding, which successfully establishes a solid physical link between the two materials. H-bonding aids in the uniform dispersion of MoS<sub>2</sub> NSs inside the PVA matrix by inhibiting agglomeration.

#### 2.4. Preparation of Thin Films

As prepared polymer NCP thin film is deposited onto the glass

substrate of 2.5 cm × 2.5 cm dimensions by utilizing drop casting method. The glass substrate has been cleaned by progressively dipping it in acetone, DI water, and then ultrasonically cleaning it for 30 min at a time. As deposited thin film has been dried under the lamp for 3–4 h to get the solvent to evaporate completely.

#### 2.5. Photomemristive device fabrication

Fluorine doped tin oxide (FTO) glass substrate of dimensions 1.5 cm × 1.5 cm has been used here as a conducting electrode. First of all, we have done the cleaning of substrate ultrasonically by dipping into acetone, methanol and DI water sequentially and sonicating for 30 min. each. Then we have deposited thin film of polymer NCPs onto FTO using the drop casting method and allowed drying under the lamp for 3–4 h. To carry out electrical measurements, we have deposited Ag electrodes and allowed them to dry completely. For I-V measurements, the bottom contact has been taken from FTO and the top contact has been taken from the Ag electrode. Fig. 3 depicts the schematic of device fabrication.

#### 3. Characterization techniques

Structural characterization of the synthesized MoS<sub>2</sub> NSs and MoS<sub>2</sub>/PVA NCPs has been carried out using an X-ray diffractometer (PAN analytical X'Pert PRO X-ray diffractometer) within the 2θ range: 15–60° to get the information regarding the sample's crystallinity. FESEM has been utilized to get information regarding the morphology of the synthesized NSs and polymer NCPs and the same has been recorded with the help of SU8000 Hitachi-PU setup at 5KV accelerating voltage. The linear absorption spectrum of the synthesized NSs has been recorded in the wavelength range of 400–800 nm with the help of LABINDIA UV 3000+ spectrophotometer. The emission spectrum of the synthesized NSs in the wavelength range of 570–610 nm is obtained using the Shimadzu spectrophotofluorophotometer RF-6000 with 450 nm as the excitation wavelength. Raman spectra have been recorded. The FEI TECNAI G 20 is utilized to capture SAED patterns and HRTEM scans. Its power range is 10–200 kV, and its point resolution is 0.27 nm. The RAMAN spectrum has been recorded via a confocal RAMAN spectrometer, Renishaw within the range 340–450 cm<sup>-1</sup> using a 514 nm diode laser. The cyclic I-V measurements, endurance cycles and Write-Read-Erase-Read (WRER)

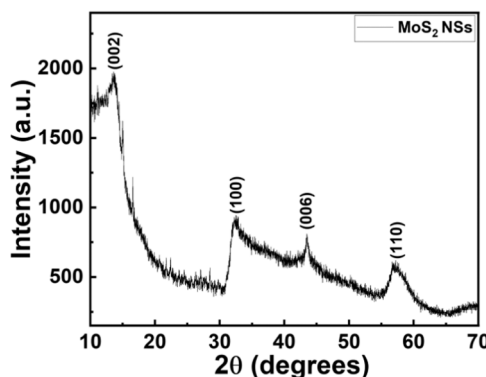


**Fig. 4.** XRD spectra of as synthesized few layered nanosheets.

measurements have been done with the help of computer operated KEITHLEY 6517A electrometer with and without light. The light source used here is a halogen lamp (200 W), whose light intensity is 1235 lx. All the electrical measurements have been done in a vacuum of the order of  $2 \times 10^{-3}$  mbar.

#### 4. Results and discussions

##### 4.1. X-ray diffraction (XRD)

**Fig. 4** displays the XRD diffractograph of as synthesized MoS<sub>2</sub> NSs. It shows prominent diffraction peaks at  $2\theta = 13.9^\circ$ ,  $32.75^\circ$ ,  $43.62^\circ$  and  $57.45^\circ$  corresponding to (002), (100), (006) and (110) hkl planes. It has been observed that the hexagonal (2 H) phase and crystalline NSs have been synthesized and the XRD data matches well with the JCPDS card No. (00-037-1492) as observed from literature. This validates that the MoS<sub>2</sub> NSs have been successfully synthesized. The broadness of the peaks is due to the quantum confinement effect and it further, indicates that the synthesized NSs are few layered just like grapheme sheet [21–24]. For the hexagonal structure with  $a = b \neq c$ , the lattice parameters of the unit cell have been determined using Eq. (1) [25]

$$\frac{1}{d^2} = \frac{4}{3} \left( \frac{h^2 + hk + k^2}{a^2} \right) + \frac{l^2}{c^2} \quad (3)$$

Where  $h$ ,  $k$ , and  $l$  are the Miller indices that correspond to the lattice planes, and  $d$  is the interplanar separation. The calculated values of lattice parameters are  $a = b = 3.14 \text{ \AA}$  and  $c = 12.42 \text{ \AA}$ . According to the literature, the standard values of lattice parameters for MoS<sub>2</sub> NSs are  $a = b = 3.16 \text{ \AA}$  and  $c = 12.30 \text{ \AA}$  [26]. The values of lattice parameters  $a = b$  and  $c$  are shifted by  $-0.02 \text{ \AA}$  and  $+0.12 \text{ \AA}$ , respectively.

The formulas listed below are used to determine the numerous structural parameters, including crystallite size ( $D$ ), dislocation density ( $\rho$ ), lattice strain ( $\epsilon$ ), stacking faults ( $\alpha$ ) and interplanar spacing ( $d$ ) [27]

$$D = \frac{0.9 \lambda}{\beta \cos \theta} \text{ (Debye – Scherer formula)} \quad (4)$$

$$\rho = \frac{1}{D^2} \quad (5)$$

$$\epsilon = \frac{\beta \cot \theta}{4} \quad (6)$$

$$\alpha = \frac{2 \pi^2 \beta}{45 \sqrt{3} \tan \theta} \quad (7)$$

$$2ds \sin \theta = n\lambda \text{ (Bragg's Law)} \quad (8)$$

Where  $\beta$  is the diffraction peak's FWHM,  $\lambda$  is the incident Cu K $\alpha$  radiations wavelength,  $d$  is the interplanar spacing, and  $\theta$  is Bragg's angle.

**Table 2**

Lattice Parameters for as synthesized few layered MoS<sub>2</sub> NSs.

Sr. No.	$2\theta (\text{°})$	$d(\text{\AA})$	$D(\text{nm})$	$\alpha (\times 10^{-3})$	$\epsilon (\times 10^{-3})$	$\rho (\times 10^{11})$
1.	13.90	6.36	10.68	9.47	26.79	08.76
2.	32.75	2.72	09.47	7.12	12.97	11.13
3.	43.62	2.07	17.13	3.48	05.44	03.40
4.	57.45	1.60	05.69	9.49	12.66	30.85

The calculated value of all the structural parameters for the as synthesized MoS<sub>2</sub> NSs is provided in **Table 2**.

#### 4.2. Optical properties

##### 4.2.1. UV-Vis spectroscopy

The UV-Vis absorption spectrum of as synthesized few layered MoS<sub>2</sub> NSs is given in **Fig. 5(a)**. We have observed that the spectra show three absorption peaks marked as A (711 nm), B (624 nm) and C (511 nm). The peaks that correspond to A (~1.74 eV) and B (~1.98 eV) show the direct band transitions of the MoS<sub>2</sub> NSs and originated due to the transition at the K-point of the Brillouin zone between the valence and conduction band edges. The two absorption peaks at A and B are the two characteristic peaks of a few layered MoS<sub>2</sub> NSs. Thus, the successful synthesis of MoS<sub>2</sub> NSs is confirmed by the absorption spectra. The transition between the states that exist deeper within the valence band and the conduction band is linked to the absorption band corresponding to mark C (~2.42 eV) [28].

The Tauc plot has been used to determine the band gap energy of synthesized few layered MoS<sub>2</sub> NSs. The following equation is used to calculate the band gap energy [29]

$$\alpha h\nu = A(h\nu - E_g)^n \quad (9)$$

Where  $\alpha$  is the linear absorption coefficient,  $h\nu$  is the energy of incident photon and  $E_g$  is the calculated value of band gap energy. MoS<sub>2</sub> is direct band gap material so  $n$  will take value 1/2 [30]. The  $(\alpha h\nu)^2$  v/s  $h\nu$  plot is given in the inset of **Fig. 5(a)**. The calculated band gap for the synthesized MoS<sub>2</sub> NSs comes out to be 1.62 eV and this corresponds well with the value observed in the literature [31].

##### 4.3. PL spectroscopy

**Fig. 5(b)** shows the PL emission spectrum for the as synthesized MoS<sub>2</sub> NSs. It has been reported earlier in literature that the bulk MoS<sub>2</sub> does not show any characteristic PL emission peak, but as the thickness of MoS<sub>2</sub> is reduced from 3D bulk to 2D NSs, the characteristic PL emission peaks starts to appear in the PL spectrum and the PL emission wavelength blue shift's with the decrease in number of layers present [32]. The spectrum shows three emission peaks marked as A (~677 nm), B (~634 nm) and C (~592 nm). The distinctive excitonic emission peaks of a few layered MoS<sub>2</sub> NSs are shown by peaks corresponding to mark A and mark B [33, 34]. The direct emission from the deep levels of the conduction band to the shallow states of the valance band is represented by the peak at point C. The two peaks corresponding to mark A and B are the two characteristic peaks of few layered MoS<sub>2</sub> NSs in accordance with the literature [35]. The energy difference between the two excitonic peak positions A (1.83 eV) and B (1.95 eV) is 0.12 eV, which matches well with the previously reported values for direct band gap MoS<sub>2</sub> NSs [32]. It has been observed that the PL emission peaks occur at lower wavelength than the excitonic absorption peaks discussed earlier in **Section 4.2.1**. This shift in the emission peak wavelength to lower side occurs due to the quantum confinement effect. The quantum confinement effect restricts the movement of charge carriers thus resulting in the variations in the electron distribution which inturn shifts the PL emission to lower wavelength than that of UV absorption wavelength in case of MoS<sub>2</sub> NSs [36–38].

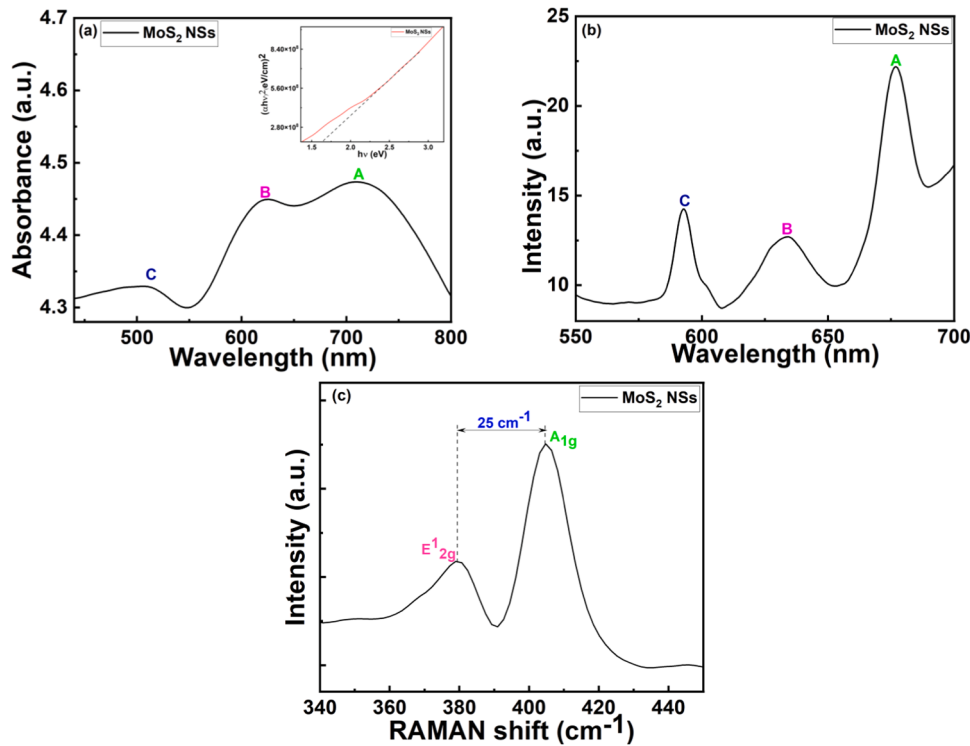


Fig. 5. (a) Absorption spectrum (Inset Tauc plot) (b) PL emission spectrum and (c) RAMAN spectrum of as synthesized MoS<sub>2</sub> NSs.

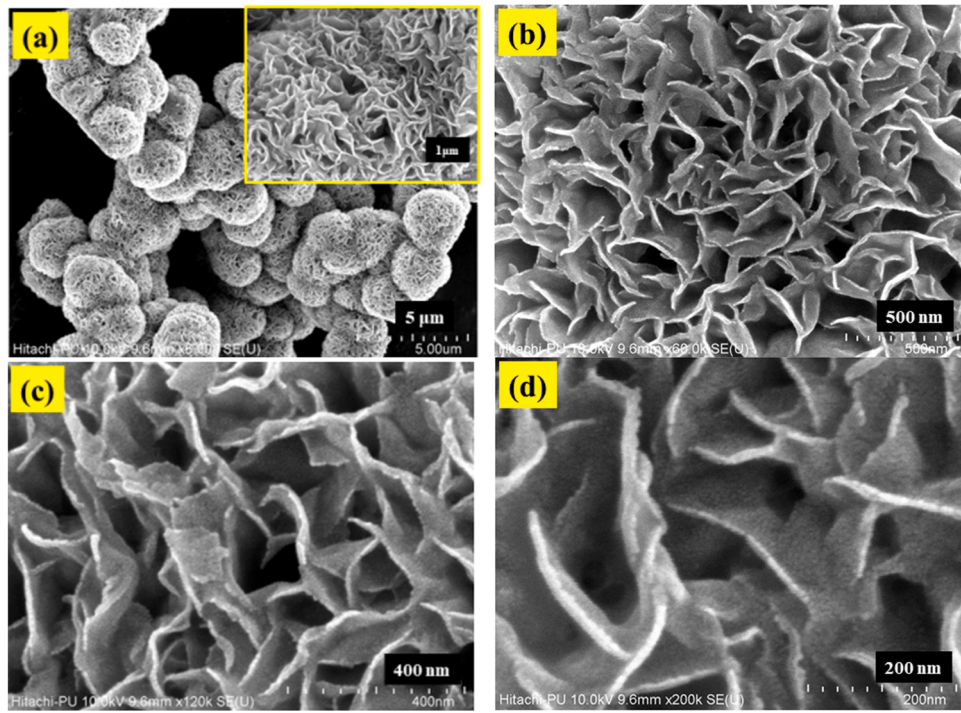
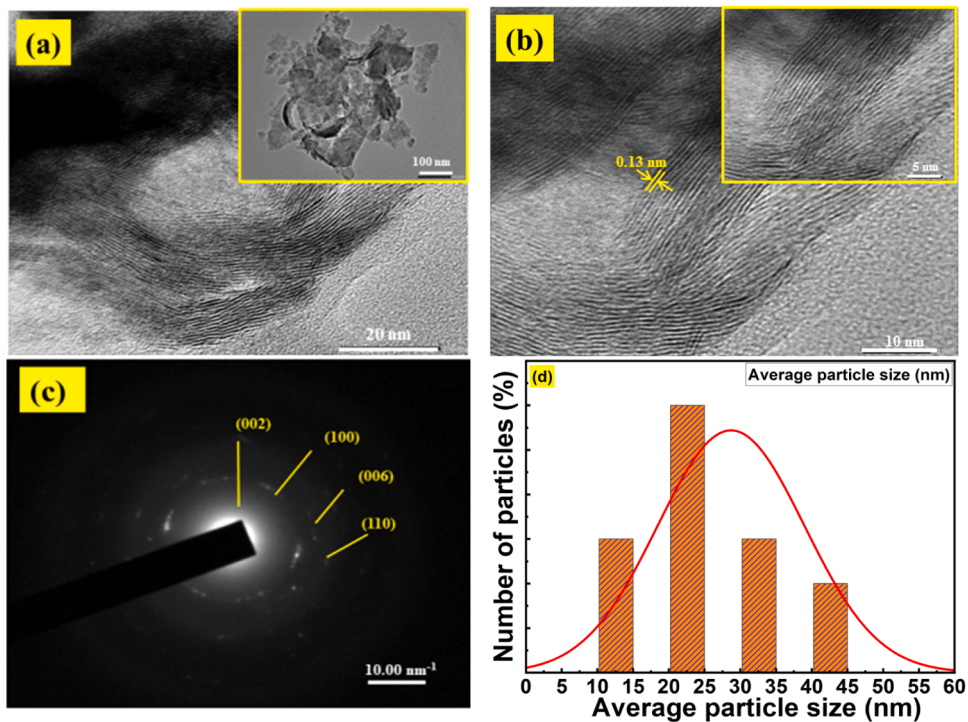


Fig. 6. FESEM scans of MoS<sub>2</sub> NSs at (a) 5 μm (inset shows at 1 μm magnification) (b) 500 nm (c) 400 nm and (d) 200 nm magnification.

#### 4.3.1. RAMAN spectroscopy

The RAMAN spectrum gives information regarding the various vibrational modes of a material. This is the most reliable and powerful technique to estimate the number of layers inside a layered material. The RAMAN spectrum of as synthesized MoS<sub>2</sub> NSs is given in Fig. 5(c). The spectrum shows the two vibrational modes: one is due to in-plane vibrations of S and Mo atoms in opposite direction and the other is

due to out of plane vibrations of S atoms. The former vibrations are marked as E<sub>2g</sub><sup>1</sup> (379 cm<sup>-1</sup>) and the latter vibrations are marked as A<sub>1g</sub> (404 cm<sup>-1</sup>). The number of layers in a few layered MoS<sub>2</sub> can be estimated by the frequency difference ( $\Delta\omega$ ) between E<sub>2g</sub><sup>1</sup> and A<sub>1g</sub> vibrational modes. In our case, the value of  $\Delta\omega \sim 25$  cm<sup>-1</sup> and this difference confirms the presence of four layers (quadrilayer) within the synthesized few layered MoS<sub>2</sub> NSs in accordance with the literature [36,39,40].



**Fig. 7.** HRTEM images (a) at 20 nm (inset shows image at 100 nm) (b) at 10 nm (inset shows image at 5 nm) (c) SAED pattern and (d) particle size distribution of as synthesized few layered MoS<sub>2</sub> nanosheets.

#### 4.4. FESEM

**Fig. 6** shows the high resolution FESEM scans of as synthesized few layered MoS<sub>2</sub> NSs at different magnifications. **Fig. 6(a)** shows the spherical morphology of synthesized MoS<sub>2</sub> due to which one can thought that the MoS<sub>2</sub> NPs have been synthesized but as we move towards the FESEM scans at higher magnification (Inset of **Fig. 6(a)**), we observed that this spherical morphology is due the nanospheres formed

by the stacking of 2D NSs. The layered structure of MoS<sub>2</sub> NSs is appears to be flaky and the layers are arranged in a compact way.

**Fig. 6(a)** shows that the various NSs are uniform and stacked together to form a cluster of nanospheres. Each nanosphere consists of a nano-flower type superstructure. The thin NSs of a few layered MoS<sub>2</sub> are curved and packed themselves densely in the form of petals of that nanoflower. Thus, the synthesized sample has uniform nanoflower type morphology. The hydrothermal reaction between sodium molybdate

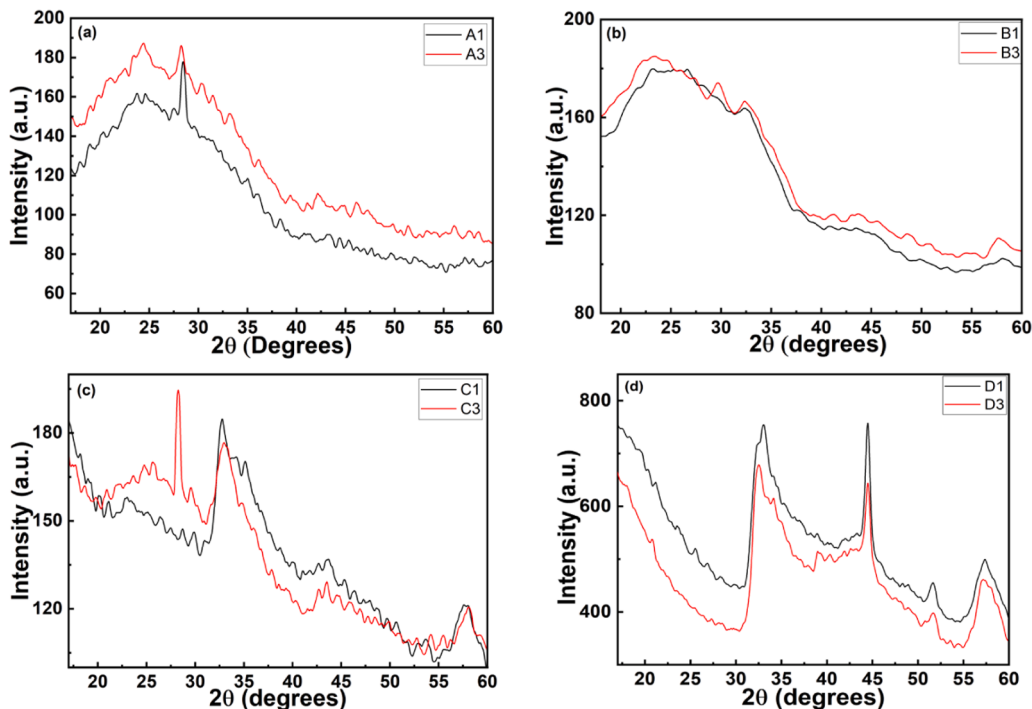


**Fig. 8.** XRD spectra of (a) A1, A3 (b) B1, B3 (c) C1, C3 (d) D1, D3 [14].

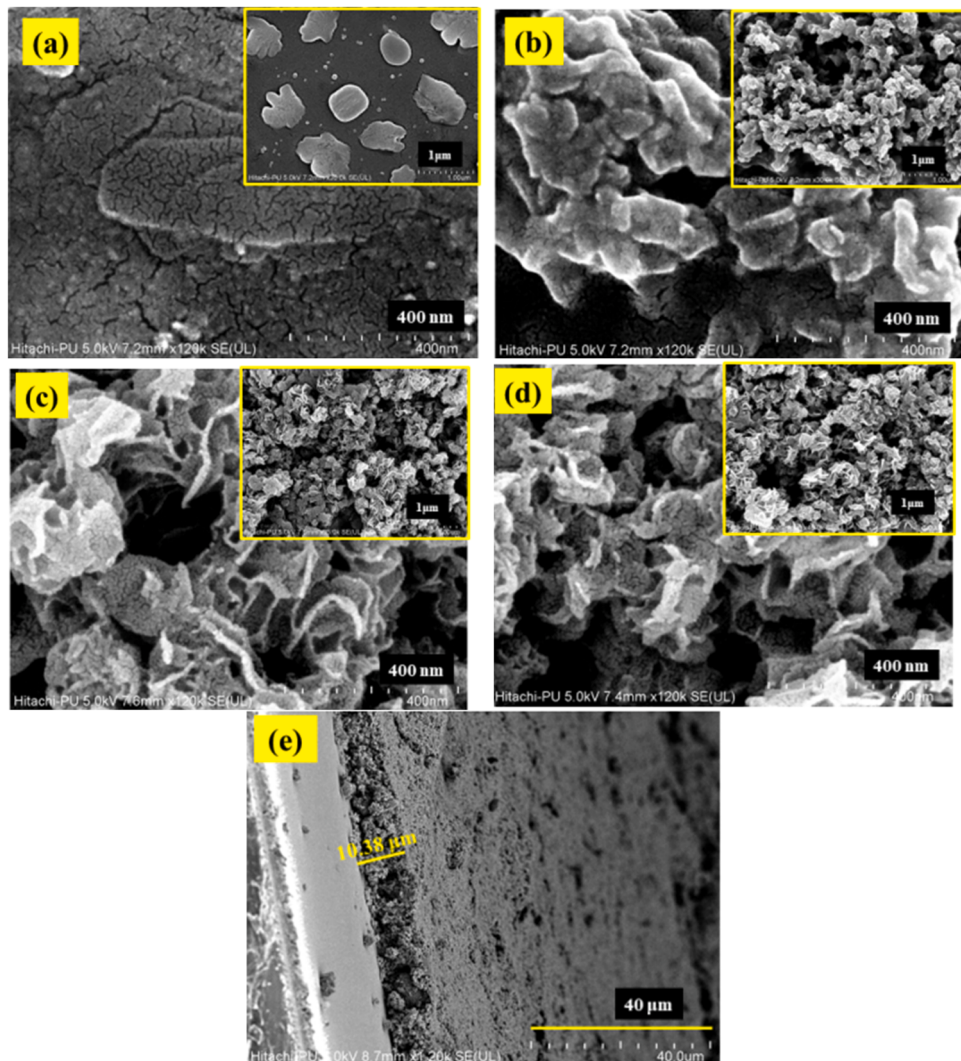


**Fig. 9.** FESEM scans of (a) A1 (b) A3 (c) C1 (d) C3 at 500 nm (Inset shows the FESEM scans at 1 μm) (e) cross-sectional view of C3 thin film.

and thiourea synthesized the  $\text{MoS}_2$  NPs that become the nucleation sites and on growth they form the  $\text{MoS}_2$  NSs. The 3D nanoflowers observed in the FESEM scans as shown in Fig. 6(a) are produced due to the self-assembling of these 2D NSs. It is evident from the FESEM scans that the agglomeration of NSs cause the nanoflower type morphology [41–44]. It appears from the FESEM scans Fig. 6(b), (c) and (d) that the NSs are expanding in all directions, giving the surface an uneven appearance [45].

#### 4.5. HRTEM

Fig. 7(a) and (b) shows the HRTEM images of as synthesized  $\text{MoS}_2$  NSs. We have observed from HRTEM images that the synthesized  $\text{MoS}_2$  sample consists of well-dispersed NSs. The magnified HRTEM image of the synthesized sample is given in Fig. 7(b) at a magnification of 10 nm (inset shows the image at a magnification of 5 nm).

The various planes are stacked together and the interplanar spacing between adjacent layers is 0.13 nm which corresponds to the (002) plane and the results obtained are in good agreement with the XRD results as discussed earlier in Section 4.1 [21]. Further, the observed morphology of  $\text{MoS}_2$  NSs is in good agreement with the results obtained from FESEM images discussed earlier in Section 4.3. Fig. 7(c) shows the selected area electron diffraction (SAED) pattern of  $\text{MoS}_2$  NSs. Various diffraction ring patterns can be clearly observed in Fig. 7(c) and this confirms the crystalline nature of the synthesized sample [46]. These

diffraction rings correspond to (002), (110), (006) and (110) crystalline planes. The particle size of  $\text{MoS}_2$  NSs as calculated using Fig. 7(a) (inset) varies from 11 nm to 47 nm. The particle size distribution has been given in Fig. 7(d) [24].

#### 4.6. Device characterization

Fig. 8(a)–(c) and (d) display the XRD spectrum of A1, A3; B1, B3; C1, C3 and D1, D3. It has been noted that each sample exhibits a broad hump that corresponds to  $2\theta = 24.3^\circ$ , which is the characteristic peak of PVA [47,48].

From Fig. 8(a) and (b), we have observed that the intensity of the XRD peak increases with an increase in ultrasonication time duration for 0.1 wt% and 0.5 wt% concentration. This may be due to the fact that the linkages of  $\text{MoS}_2$  NSs with polymeric chains get enhanced which in turn increases the dispersivity of  $\text{MoS}_2$  NSs within the polymer matrix with enhancement in the ultrasonication time duration. As a result, the crystallinity of the NCPs increases with an increase in ultrasonication time duration. Fig. 8(c) and (d) shows some prominent peaks corresponding to  $2\theta = 32.7^\circ$ ,  $43.7^\circ$ , and  $57.9^\circ$  which are some of the characteristic peaks of  $\text{MoS}_2$  NSs. The diffraction peaks corresponding to  $\text{MoS}_2$  grow prominently and the peaks corresponding to PVA got diminish as the density of  $\text{MoS}_2$  NSs rises [49,50]. We have observed that for 1 wt% and 1.5 wt%, the XRD peak intensity decreases with an enhancement in the ultrasonication time duration because, for a higher

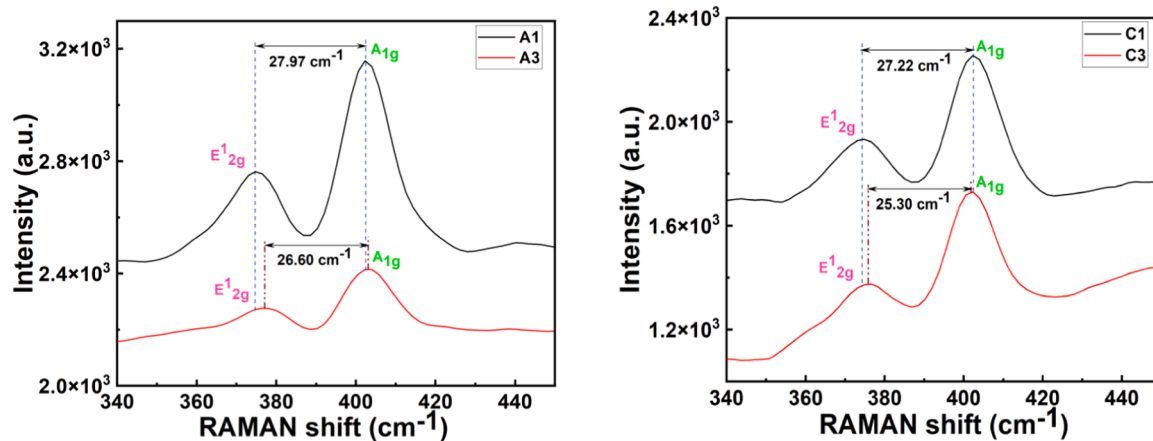


Fig. 10. RAMAN spectra of (a) A1, A3 and (b) C1, C3.

concentration of NSs within the polymer matrix, the effect of ultrasonication on the MoS<sub>2</sub> NSs becomes more conspicuous. The MoS<sub>2</sub> layers got exfoliated expeditiously. The process of exfoliation causes the crystal lattice to weaken or be disrupted and results in the production of thinner layers causing the XRD peak intensity to decline [51].

Fig. 9(a)–(d) shows the FESEM morphological scans of A1, A3, C1 and C3 at 400 nm magnification, respectively. The inset shows the FESEM scan at a magnification of 1 μm. It is clear from the FESEM scans that the NCPs exhibit nanoflower type morphology. They have porous morphology and there is also cluster formation. After comparing the FESEM results in Fig. 9(a)–(d), at different concentration of MoS<sub>2</sub> in PVA shows that sonication improved the dispersion of NSs inside the polymer matrix.

We have observed from Fig. 9(a) and (b) that for a lower concentration of MoS<sub>2</sub> (0.1 wt%) within the polymer matrix, the NSs are not clearly visible for 30 min. of sonication but as the sonication increases upto 8 h, some of the NSs in form of nanopetals starts appearing clearly due to exfoliation. The exfoliation of the NSs got enhanced with ultrasonication and this result is in accordance with the RAMAN spectrum as discussed later in this section.

For higher concentration of MoS<sub>2</sub> (1 wt%), the NSs in the form of nanopetals are observable even for 30 min. of sonication but they become visible more prominently with enhancement in ultrasonication time duration upto 8 h as seen from Fig. 9(c) and (d). The ultrasonication enhances the dispersivity of NSs within the polymer matrix as well as expedites the process of exfoliation of NSs as explained earlier in this section [52–54]. Fig. 9(e) shows the cross-sectional view of a thin film of C3. The deposited thin film has a layer thickness of ~ 10.38 μm.

Fig. 10(a) and (b) display the RAMAN spectra of A1, A3 and C1, C3. We have observed from Fig. 10(a) and (b) that as the ultrasonication time duration increases, the Δk value decreases from 27.97 cm<sup>-1</sup> (A1) to 26.60 cm<sup>-1</sup> (A3) and 27.22 cm<sup>-1</sup> (C1) to 25.30 cm<sup>-1</sup> (C3). The Δk values are the fingerprint of the number of layers inside a layered material. The decrease in Δk value indicates that the exfoliation of NSs got enhanced and results to a decline in the number of layers. This result is in agreement with the FESEM scans and literature study [36,40,55]. From FESEM results (Fig. 10(c) and (b)), it is clearly observed that the petals of nanoflower, which are the stacked 2D NSs are clearly observable with an enhancement in the ultrasonication time duration.

From Fig. 10(a) and (b), we have further observed that the intensity of the E<sub>2g</sub><sup>1</sup> absorption band goes on decreasing and FWHM of the same goes on increasing as the concentration of MoS<sub>2</sub> NSs as well the ultrasonication time duration increases. The decrease in peak intensity and broadening of the peak may arise due to the loss of sulfur and the occurrence of sulfur vacancies within the polymer NCPs. We have further observed that with an increase in concentration of MoS<sub>2</sub> NSs as well as an increase in ultrasonication time duration, more and more

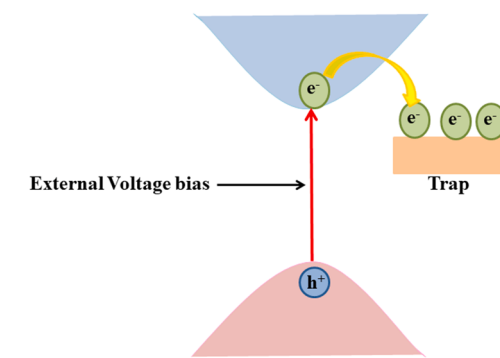


Fig. 11. Schematic of charge trapping by the trap states responsible for electrical hysteresis.

surface defects got introduced [19,56].

We have examined the I-V measurements of the device with the help of the KEITHLEY 6517A model in the absence as well as in the presence of light. The electrical hysteresis represents the charge storage by the samples. As we apply the external voltage bias, the electrons jump from conduction band to valance band creating a hole within the valance band. After sometime, the electrons relax back to the ground state, but on their way they got trapped by the trap states due to various defects present. This trapping of electrons by the trap states is responsible for the electrical hysteresis shown by the samples (as depicted by Fig. 11). Figs. 12–15 shows the semi-logarithmic I-V plots in the absence of external light for Ag/MoS<sub>2</sub>-PVA/FTO device with 0.1 wt%, 0.5 wt%, 1 wt% and 1.5 wt% of MoS<sub>2</sub>/PVA NCPs (active layer), respectively. We have examined the hysteresis behavior (bipolar resistive switching behavior) of the fabricated device over three successive cycles with a voltage sweeping loop of -5 V → 0 V → 5 V → 0 V → -5 V. The stability and reproducibility of the device is shown by the negligible loss of stored data over the three successive cycles as observed from the I-V hysteresis loop [57].

We have observed from the semi-logarithmic I-V plots that as the voltage rises upto 0.5 V, the current starts to rise suddenly and this process is known as the SET process (non-volatile ON state) and the corresponding voltage is known as "V<sub>SET</sub>". At V<sub>SET</sub>, the device got switched from a high resistance state (HRS) to a low resistance state (LRS). The device got switched from LRS to HRS as the voltage reaches -0.5 V and this process is known as RESET (non-volatile OFF state) and the corresponding voltage is known as "V<sub>RESET</sub>". The two states i.e.; SET and RESET states are regarded as "read" and "write" states of the memristive device. Thus, the device may be switched between two conductivities at a specific voltage by just changing the polarity of the

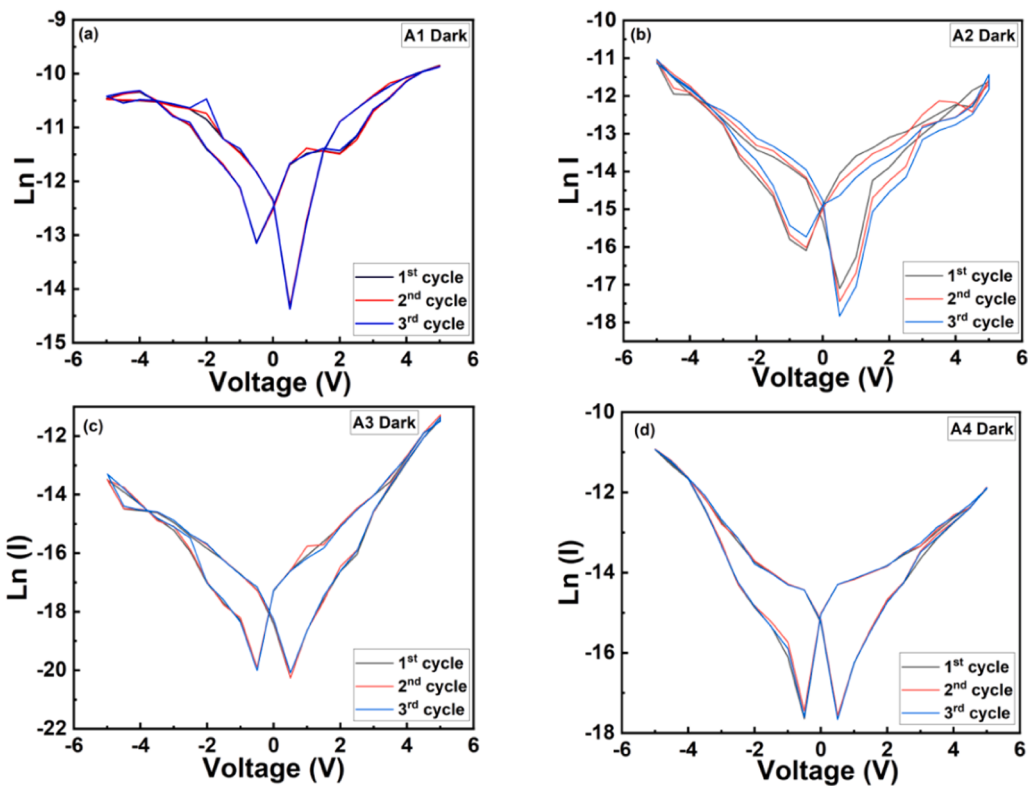


Fig. 12. Semi logarithmic I-V curve for (a) Ag/A1/FTO (b) Ag/A2/FTO (c) Ag/A3/FTO and (d) Ag/A4/FTO device in dark.

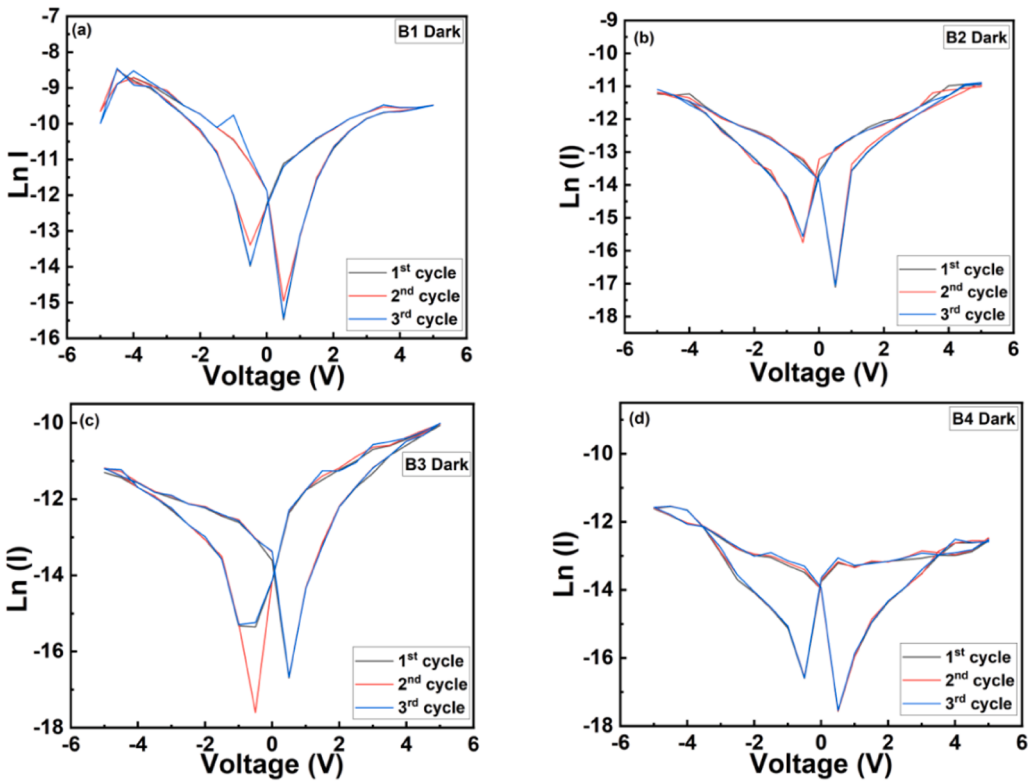


Fig. 13. Semi logarithmic I-V curve for (a) Ag/B1/FTO (b) Ag/B2/FTO (c) Ag/B3/FTO and (d) Ag/B4/FTO device in dark.

applied bias, as demonstrated by the symmetrical hysteresis loop [58, 59]. In the present study, we have enhanced the as synthesized photo-memristive device's performance by altering the concentration of NSs

within the polymer matrix as well as by altering the ultrasonication time duration.

The resistive switching mechanism could be explained by various

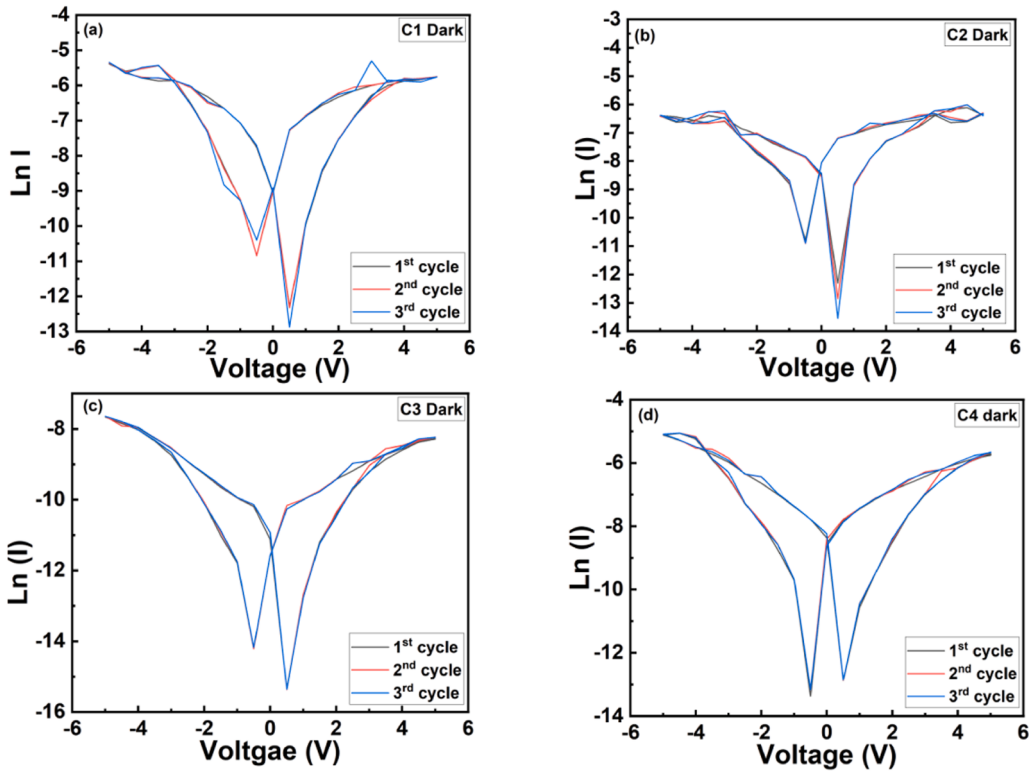


Fig. 14. Semi logarithmic I-V curve for (a) Ag/C1/FTO (b) Ag/C2/FTO (c) Ag/C3/FTO and (d) Ag/C4/FTO device in dark.

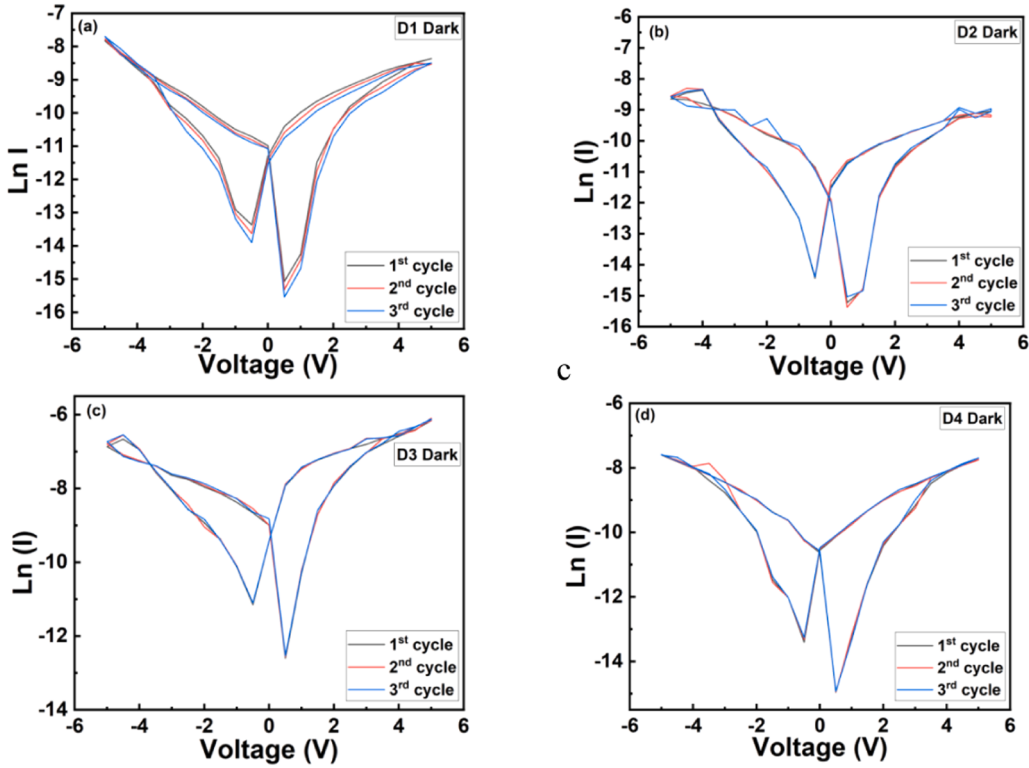


Fig. 15. Semi logarithmic I-V curve for (a) Ag/D1/FTO (b) Ag/D2/FTO (c) Ag/D3/FTO and (d) Ag/D4/FTO device in dark.

mechanisms but in our case conductive bridge random access memory (CBRAM) mechanism is responsible for the resistive switching due to the presence of conducting silver (Ag) as the top electrode. This mechanism encompasses the formation and dissolution of conductive filament (CF)

[60].

As we apply forward bias, the ionization of Ag atoms occurs to produce  $\text{Ag}^+$  ions and a free electron. The  $\text{Ag}^+$  will drift in the direction of the applied electric field i.e. towards the FTO and the  $e^-$  will drift in

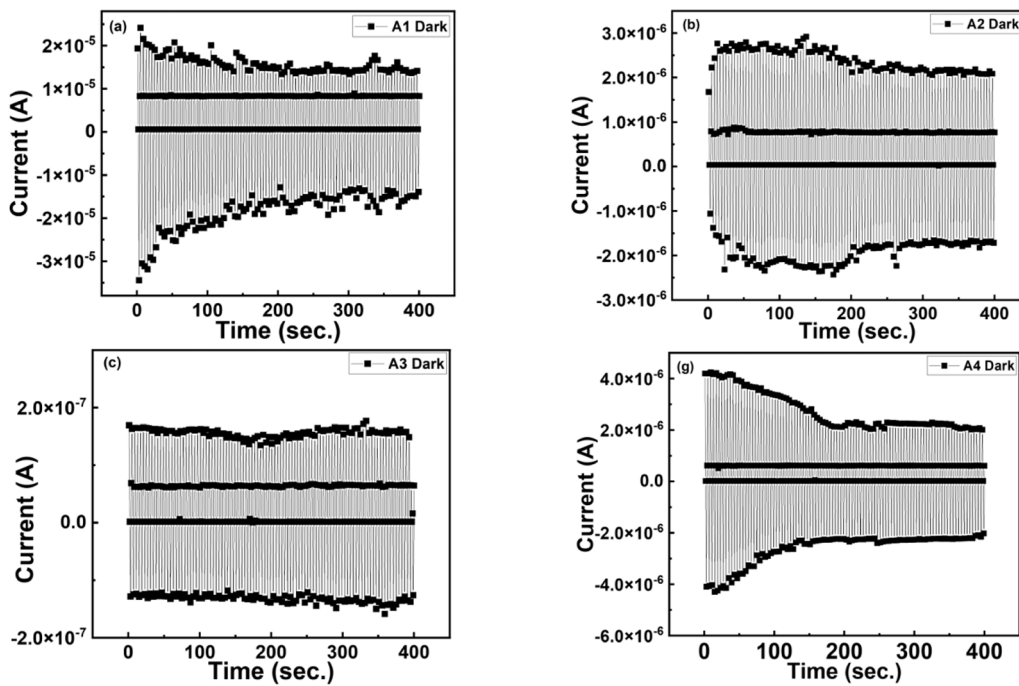


Fig. 16. WRER cycles for (a) Ag/A1/FTO (b) Ag/A2/FTO (c) Ag/A3/FTO and (d) Ag/A4/FTO device in dark.

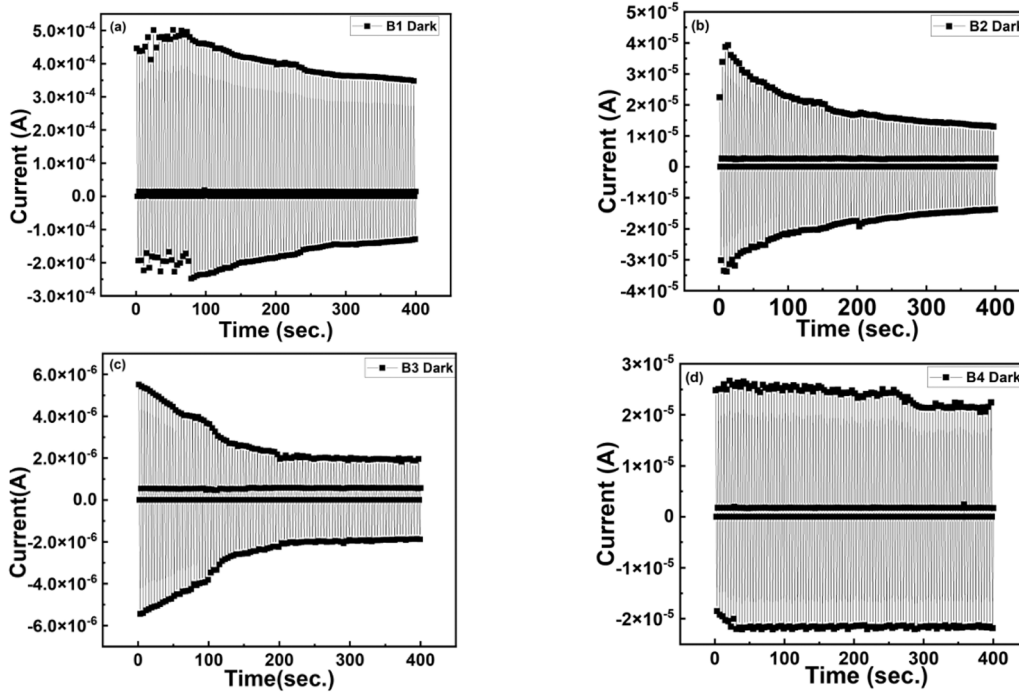


Fig. 17. WRER cycles for (a) Ag/B1/FTO (b) Ag/B2/FTO (c) Ag/B3/FTO and (d) Ag/B4/FTO device in dark.

the direction opposite to the applied field i.e. towards the Ag electrode. As a result, an internal electric field will be developed in the opposite direction of the applied electric field. The incorporation of  $\text{Ag}^+$  ions within the active layer enhances its conductivity and this process is known as the formation of conductive filament. The migration of  $\text{Ag}^+$  ions and a free  $e^-$  will continue until the induced field becomes equal to the applied field. At this stage, the device is known to be in the "SET" position or "ON" state (LRS). The device will remain in the LRS state until a negative bias is applied. The induced internal electric field starts to decrease as we decrease the external bias upto 0 V and  $\text{Ag}^+$  ions start

drifting back toward the Ag electrode. The CF got ruptured on applying negative bias and this process is known as dissolution of CF. At this condition device is said to be in the "RESET" position or "OFF" state (HRS). The device will remain in the HRS state until the applied negative bias returns back to 0 V. On further applying the positive bias the device again undergoes LRS state due to formation of CF and on applying negative bias it undergoes HRS state and the whole process is repeated again and again [61–63]. In our case, the active layer is  $\text{MoS}_2/\text{PVA}$  NCP, here  $\text{MoS}_2$  is the charge trapping site and PVA prevents the leakage of stored charge. The resistive switching may also occur when charge

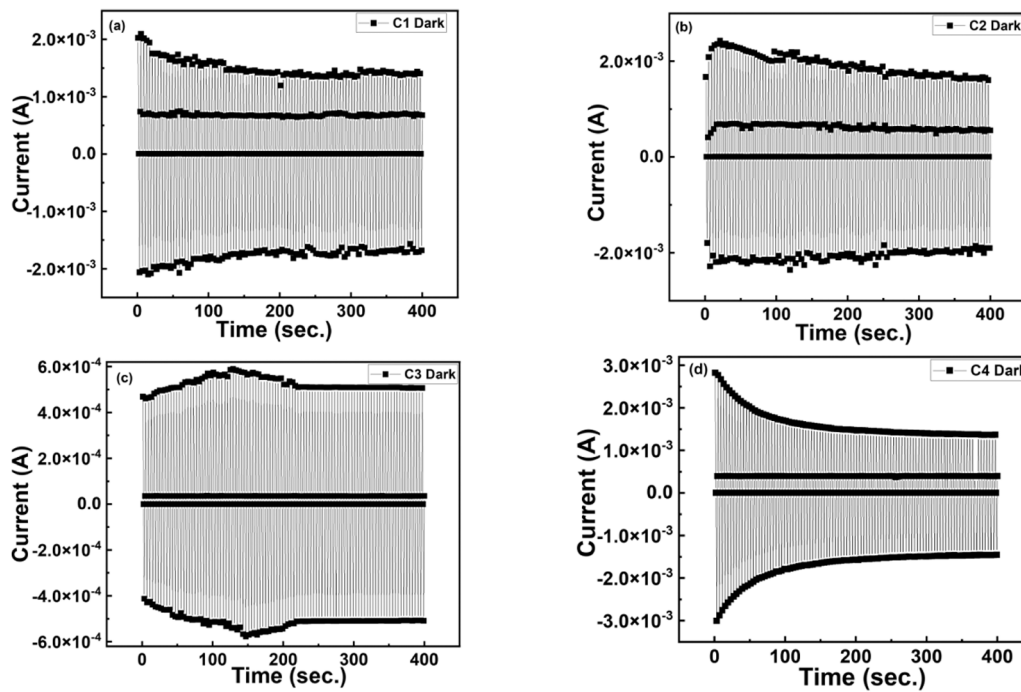


Fig. 18. WRER cycles for (a) Ag/C1/FTO (b) Ag/C2/FTO (c) Ag/C3/FTO and (d) Ag/C4/FTO device in dark.

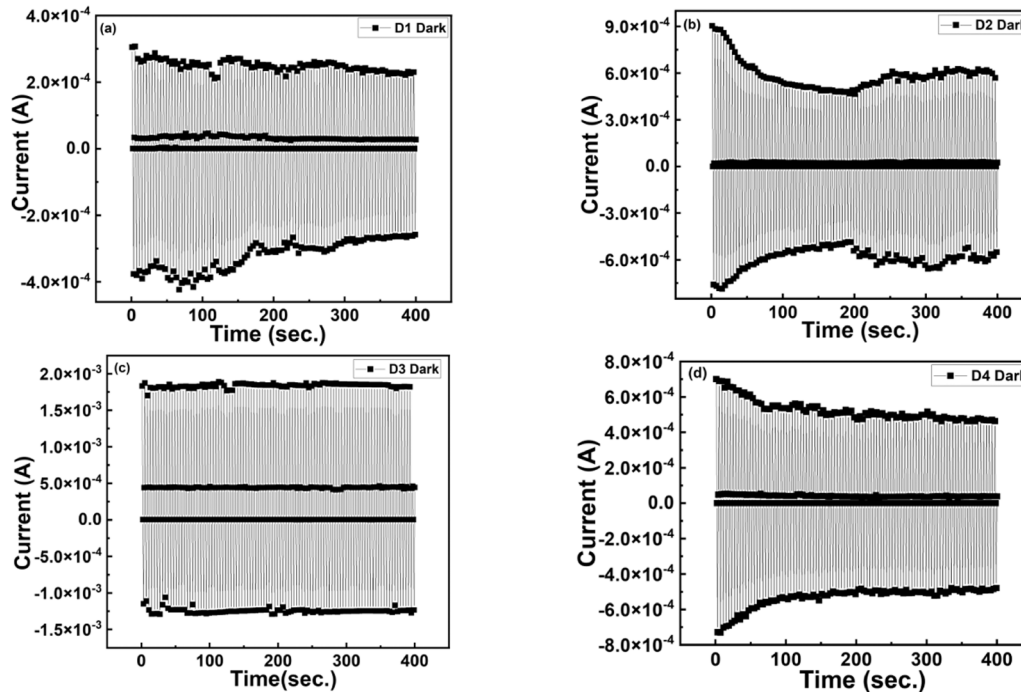


Fig. 19. WRER cycles for (a) Ag/D1/FTO (b) Ag/D2/FTO (c) Ag/D3/FTO and (d) Ag/D4/FTO device in dark.

carriers interact with the trap states present within the active layer. The electrons are present in the lower energy states in the absence of external bias and jump from lower energy states to higher energy trap states on the application of external bias voltage. At voltage  $V_{SET}$ , almost all the trap states got filled with the charge carrier and the device will switch in "SET" position. The presence of PVA in the active layer prevents the transition of charge carriers from trap states to their original states. Due to this, the device remains in the LRS state as long as we don't apply the external bias voltage in the opposite direction [63,64]. As a result, we have seen that the resistive switching behaviour is significantly

influenced by the trap states.

The standard Write-Read-Erase-Read (WRER) sequence further supports the memory characteristics, which are verified by the repetitive I-V cycles. The  $V_{SET}$  voltage for the device is 0.5 V as shown by semi-logarithmic I-V cycles. Therefore, the WRER sequence is performed at a voltage of 5 V, 0.5 V, -5V and 0.5 V over 100 cycles. Figs. 16–19 show the standard WRER sequence in the absence of an external light source for Ag/MoS<sub>2</sub>-PVA/FTO device with 0.1 wt%, 0.5 wt%, 1 wt% and 1.5 wt% of MoS<sub>2</sub>/PVA NCPs (active layer), respectively. One cycle takes 4 s to get complete and hence 100 cycles will be completed in

**Table 3**

$I_{on}/I_{off}$  values for the synthesized photomemristive device in the absence and the presence of external light source.

Sr. No.	Device	$I_{on}/I_{off}$ Ratio (Without Light)	$I_{on}/I_{off}$ Ratio (With Light)	Efficiency increase (%)
1.	Ag/A1/FTO	~14.1	~14.9	5.67
2.	Ag/A2/FTO	~20.6	~22.1	7.28
3.	Ag/A3/FTO	~39.5	~44.7	13.16
4.	Ag/A4/FTO	~28.6	~31.1	8.74
5.	Ag/B1/FTO	~79.2	~89.6	13.13
6.	Ag/B2/FTO	~81.6	~93.6	14.7
7.	Ag/B3/FTO	~89.3	~1.07 $\times 10^2$	19.82
8.	Ag/B4/FTO	~74.7	~88.2	18.07
9.	Ag/C1/FTO	~1.35 $\times 10^2$	~1.72 $\times 10^2$	27.4
10.	Ag/C2/FTO	~1.43 $\times 10^2$	~2.15 $\times 10^2$	50.3
11.	Ag/C3/FTO	~1.68 $\times 10^2$	~3.00 $\times 10^2$	77.97
12.	Ag/C4/FTO	~1.61 $\times 10^2$	~2.73 $\times 10^2$	69.56
13.	Ag/D1/FTO	~1.06 $\times 10^2$	~1.27 $\times 10^2$	19.81
14.	Ag/D2/FTO	~1.12 $\times 10^2$	~1.49 $\times 10^2$	33.03
15.	Ag/D3/FTO	~1.22 $\times 10^2$	~2.02 $\times 10^2$	65.57
16.	Ag/D4/FTO	~1.14 $\times 10^2$	~1.73 $\times 10^2$	51.75

400 s. Figs. 16–19 show current (A) v/s time (s) plot over 400 s.

The data has been written at 5 V, then read at 0.5 V, erased at -5V and again read at 0.5 V. The different values of current at the same

voltage (0.5 V) show the efficient charge storage in the device.  $I_{on}$  is the value of the device current in the LRS state and  $I_{off}$  is the value of the device current in the HRS state. The  $I_{on}/I_{off}$  ratio tells the performance of a fabricated memristive device. Table 2 displays the  $I_{on}/I_{off}$  values for all the synthesized NCPs in the absence of an external light source.

The number of trap states increases with an increase in NSs concentration (upto 1 wt%) causing  $I_{on}/I_{off}$  ratio to increase due to more and more trapping of charge carriers but the further increase in NSs concentration (upto 1.5 wt%) may cause leakage of stored charge to some extent due to lesser concentration of leakage preventing PVA polymer in comparison to conducting MoS<sub>2</sub> NSs [65,66]. Therefore, the optimized best concentration of MoS<sub>2</sub> NSs within the PVA matrix is 1 wt % for resistive switching bistable memory device applications. These results are in agreement with the RAMAN analysis of the synthesized polymer NCPs as discussed earlier in this section.

We have further investigated the effect of ultrasonication on the switching behavior of the synthesized device by measuring  $I_{on}/I_{off}$  values as listed in Table 3. We have observed that for all the concentrations of MoS<sub>2</sub> NSs within the polymer matrix, the  $I_{on}/I_{off}$  value rises with a rise in ultrasonication time duration upto 8 h and decreases thereafter (upto 12 h). The ultrasonication increases the dispersion of NSs within the PVA matrix and accelerates the drifting of Ag<sup>+</sup> ions from the top electrode to the bottom electrode on the application of external positive bias and hence enhances the  $I_{on}/I_{off}$  values [67,68]. Moreover, the diffusion length of charge carriers increases with sonication causing a decline in the frequent recombination events due to which charge carriers remain in the trap state for a longer time and hence  $I_{on}/I_{off}$  values increase with sonication [69–71]. We have obtained an optimized time duration of ultrasonication i.e. 8 h and concentration of MoS<sub>2</sub> NSs within the polymer PVA i.e. 1 wt%. The  $I_{on}/I_{off}$  value obtained for Ag/MoS<sub>2</sub>-PVA (1 wt% and 8 h sonicated)/FTO device in the absence of an external light source is ~  $1.68 \times 10^2$ , which is the highest among all the synthesized samples.

Further, we have evaluated the endurance capabilities of the fabricated device by continuously and repeatedly running the WRER sequence over 100 cycles. Figs. 20–23 display the endurance capabilities

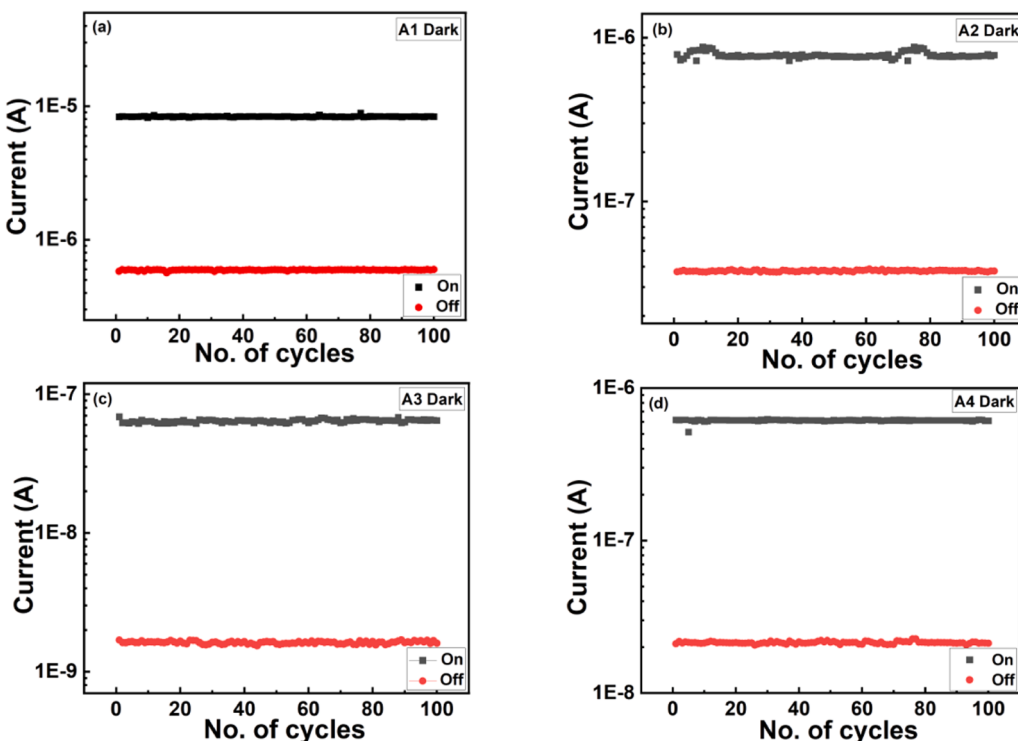


Fig. 20. Endurance characteristics for (a) Ag/A1/FTO (b) Ag/A2/FTO (c) Ag/A3/FTO and (d) Ag/A4/FTO device in dark.

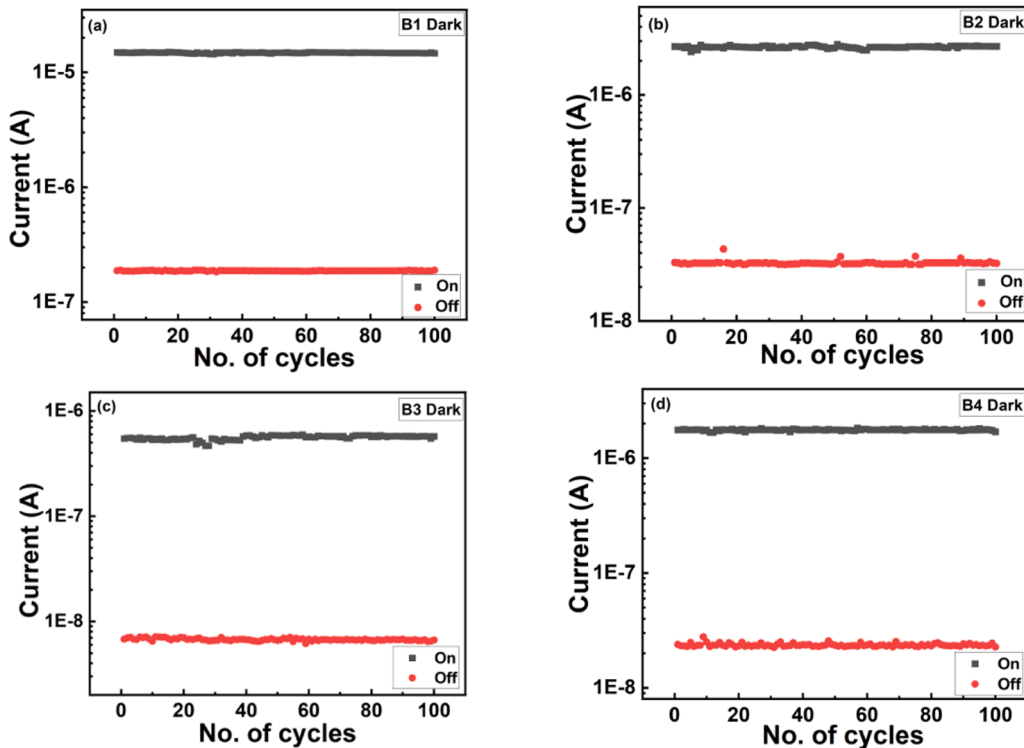


Fig. 21. Endurance characteristics for (a) Ag/B1/FTO (b) Ag/B2/FTO (c) Ag/B3/FTO and (d) Ag/B4/FTO device in dark.

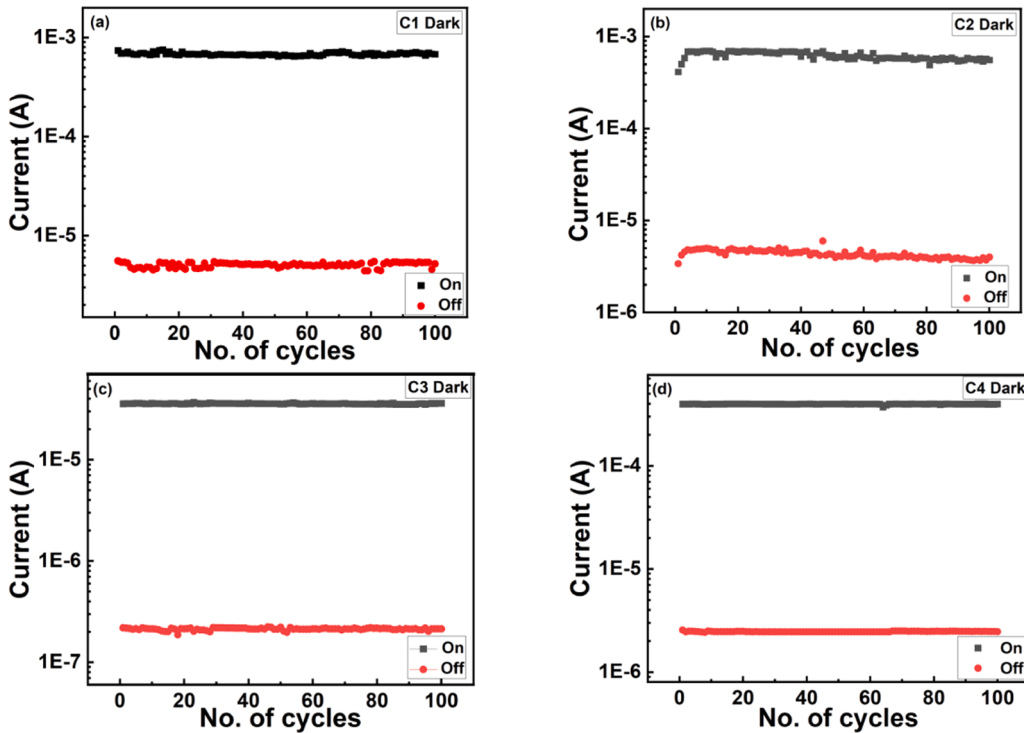


Fig. 22. Endurance characteristics for (a) Ag/C1/FTO (b) Ag/C2/FTO (c) Ag/C3/FTO and (d) Ag/C4/FTO device in dark.

in the absence of an external light source for Ag/MoS<sub>2</sub>-PVA/FTO device with 0.1 wt%, 0.5 wt%, 1 wt% and 1.5 wt% of MoS<sub>2</sub>/PVA NCPs (active layer), respectively. The endurance cycles suggest that the fabricated device does not deteriorate after 100 cycles. This proves that the device is quite reliable and has satisfactory endurance capabilities which are the relevant features of a good memristor.

The  $I_{on}/I_{off}$  ratio of a memristor can be enhanced by various means such as by using metallic dopants to increase the trap states, by making use of insulated polymer based NCPs as an active layer of memristor, by using external stimuli such as irradiating device with visible or UV radiations or with temperature, etc. The doping with metal NPs not only enhances the current ratio but also enhances the device's stability as

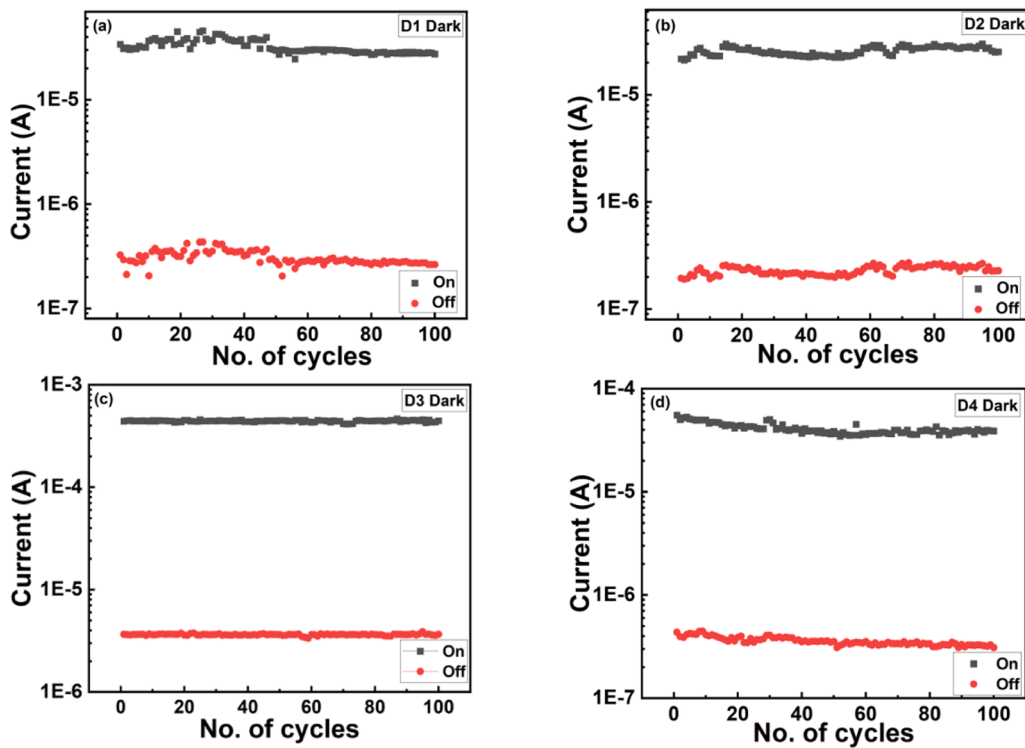


Fig. 23. Endurance characteristics for (a) Ag/D1/FTO (b) Ag/D2/FTO (c) Ag/D3/FTO and (d) Ag/D4/FTO device in dark.

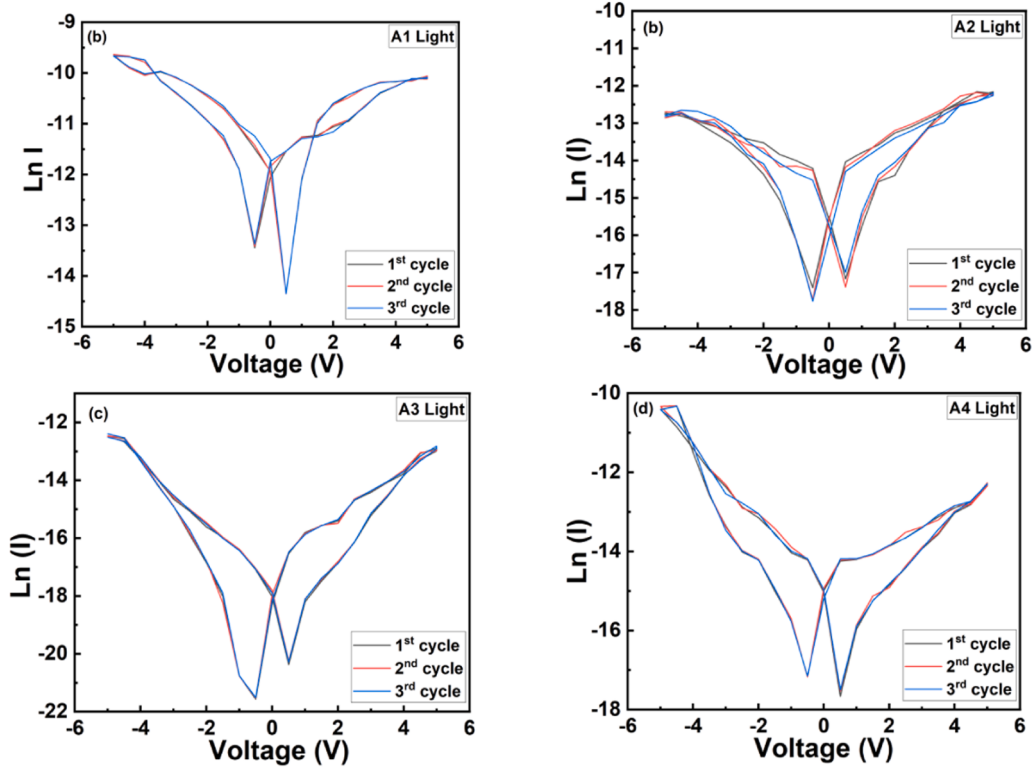


Fig. 24. Semi logarithmic I-V curve for (a) Ag/A1/FTO (b) Ag/A2/FTO (c) Ag/A3/FTO and (d) Ag/A4/FTO device in light.

well as causes lower consumption of power [72,73]. The insulating polymer can act as a hole transport layer and helps in the migration of oxygen ions and creates oxygen vacancies. These oxygen vacancies can act as trap states and enhance the performance of memristors [66]. The irradiation of the device with light can enhance the migration of ions

and hence enhance the conductivity resulting in an improvement of the memristive device [74]. From the literature, we have observed that monolayer and few layered MoS<sub>2</sub> is a photosensitive material and has a good photoresponsivity (~7.7 mA/W) [75,76]. The high photoresponsivity of MoS<sub>2</sub> motivates us to investigate the photoresponse of

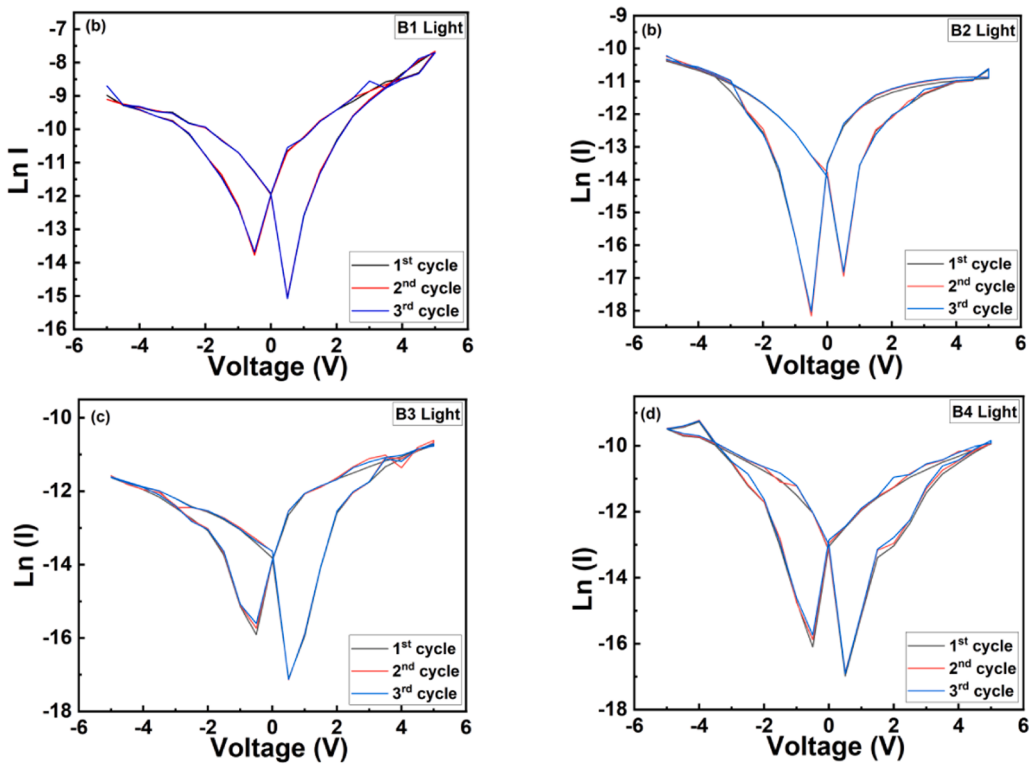


Fig. 25. Semi logarithmic I-V curve for (a) Ag/B1/FTO (b) Ag/B2/FTO (c) Ag/B3/FTO and (d) Ag/B4/FTO device in Light.

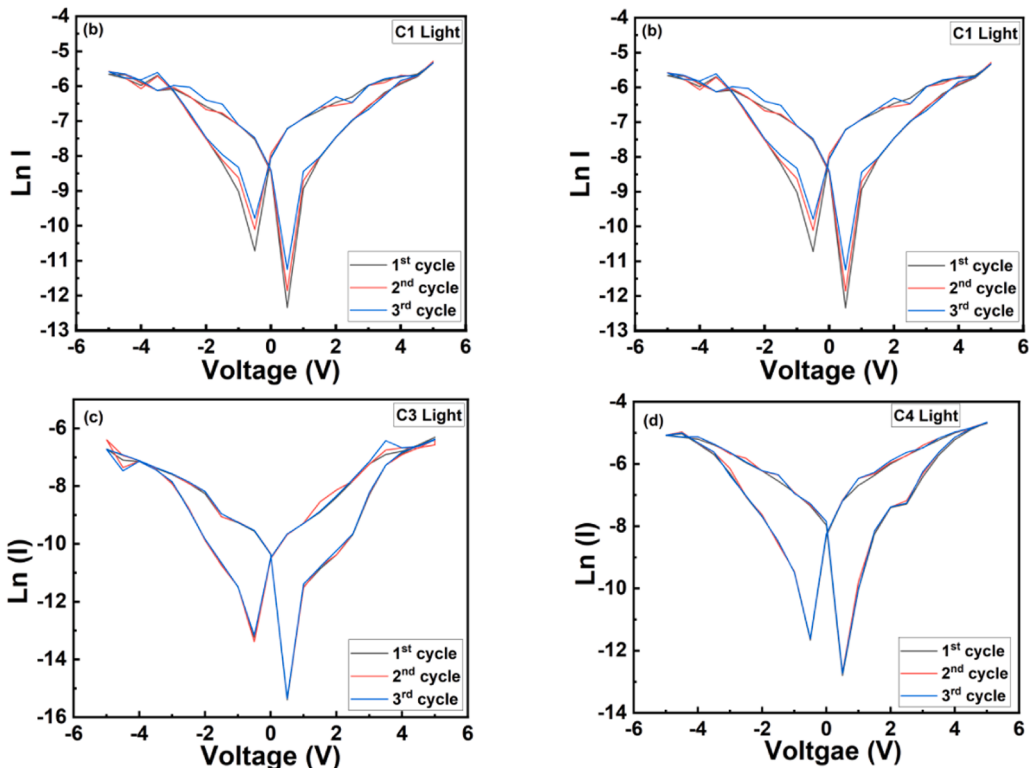


Fig. 26. Semi logarithmic I-V curve for (a) Ag/C1/FTO (b) Ag/C2/FTO (c) Ag/C3/FTO and (d) Ag/C4/FTO device in Light.

fabricated memristor with the help of light illumination [77].

In the present study, we have examined the influence of visible light on the performance of the fabricated memristive device. For this purpose, the fabricated device is placed in a vacuum and irradiated with a

light source (halogen lamp of power 200 W and light intensity 1235 lx) for 1 min and the I-V measurements are done with the help of computer operated KEITHLEY 6517 A electrometer at room temperature.

Figs. 24–27 show the cyclic I-V measurements of Ag/MoS<sub>2</sub>-PVA/FTO

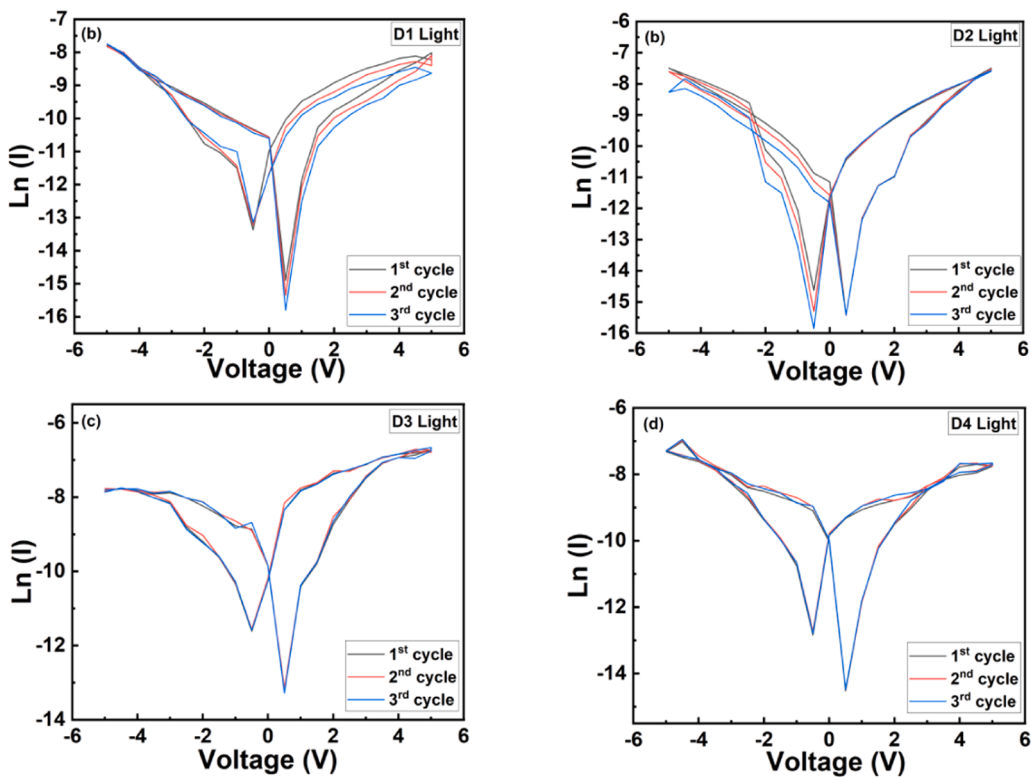


**Fig. 27.** Semi logarithmic I-V curve for (a) Ag/D1/FTO (b) Ag/D2/FTO (c) Ag/D3/FTO and (d) Ag/D4/FTO device in Light.

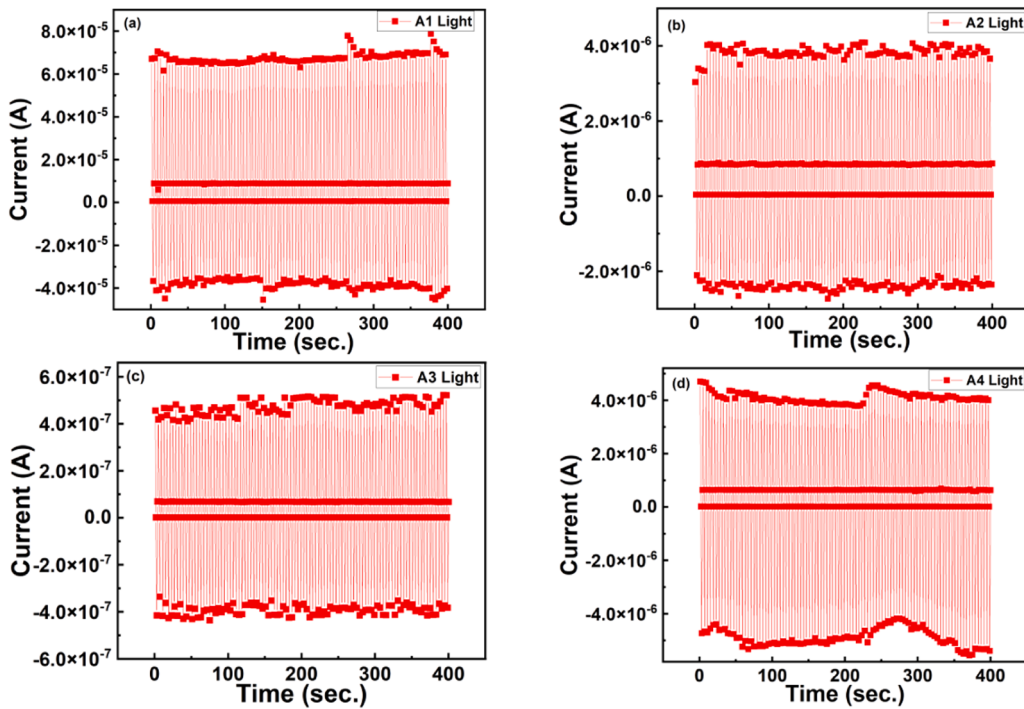


**Fig. 28.** WRER cycles for (a) Ag/A1/FTO (b) Ag/A2/FTO (c) Ag/A3/FTO and (d) Ag/A4/FTO device in light.

device in the presence of light source with 0.1 wt%, 0.5 wt%, 1 wt% and 1.5 wt% of MoS<sub>2</sub>/PVA NCPs (active layer), respectively. We have observed from the cyclic I-V measurements in the absence as well as in the presence of light that the stability and sensitivity of the manufactured photomemristive device get augmented after light irradiation. The variation of I-V is uniform for all three cycles.

We have examined the influence of light illumination on the WRER sequence over 100 cycles for an ultrasonication assisted Ag/MoS<sub>2</sub>-PVA/FTO device. Figs. 28–31 shows the WRER sequence for Ag/MoS<sub>2</sub>-PVA/FTO device with 0.1 wt%, 0.5 wt%, 1 wt% and 1.5 wt% of MoS<sub>2</sub>/PVA NCPs (active layer), respectively. We have also determined  $I_{on}/I_{off}$  values for all the synthesized samples in the presence of light. The

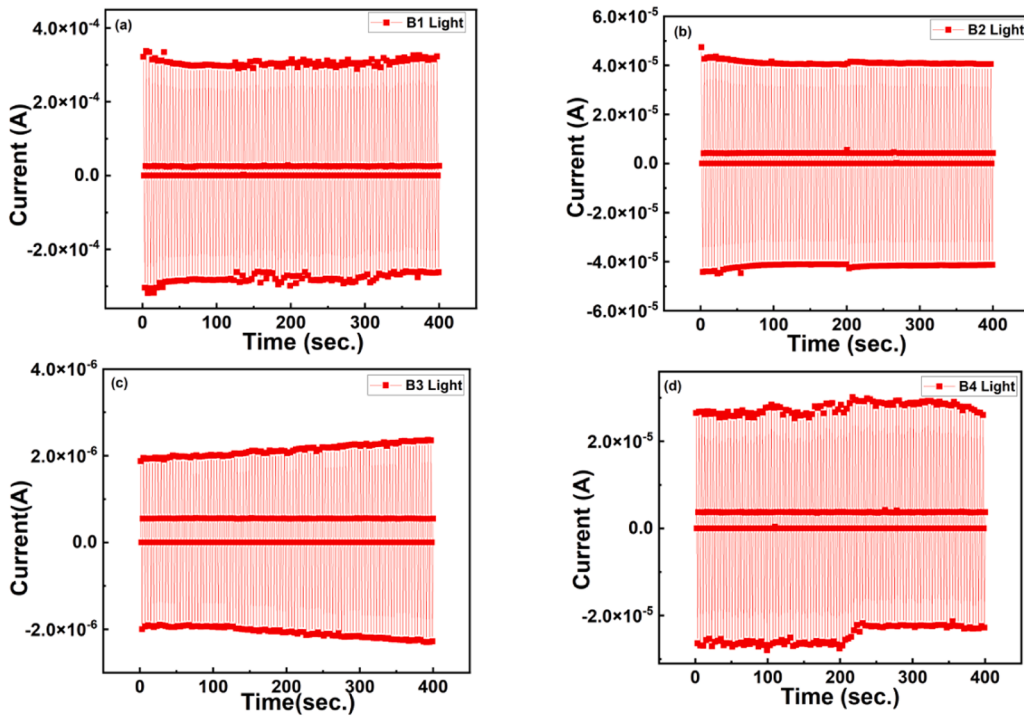


Fig. 29. WRER cycles for (a) Ag/B1/FTO (b) Ag/B2/FTO (c) Ag/B3/FTO and (d) Ag/B4/FTO device in light.

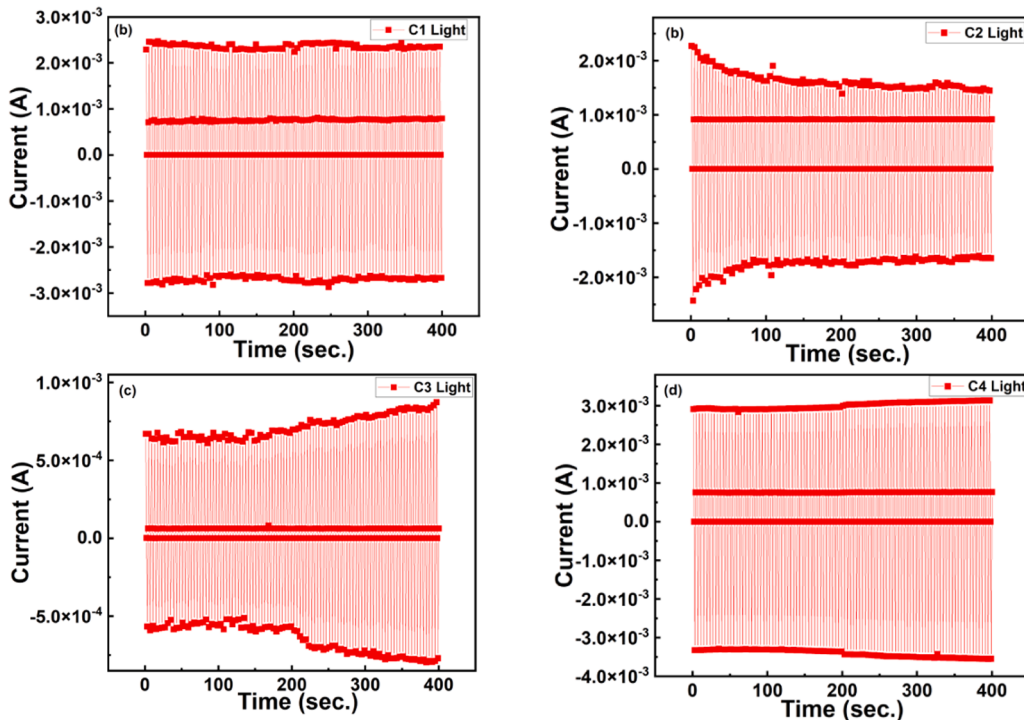


Fig. 30. WRER cycles for (a) Ag/C1/FTO (b) Ag/C2/FTO (c) Ag/C3/FTO and (d) Ag/C4/FTO device in light.

calculated  $I_{on}/I_{off}$  values and percentage increase in their values with light irradiation are also given in Table 3.

From Table 3, we have observed that the  $I_{on}/I_{off}$  values got enhanced to some extent with light as compared to their values in the absence of light for all the synthesized samples irrespective of an increase in concentration as well an enhancement in ultrasonication time duration. The reason for the same is that under light illumination, trap states may be introduced by photoinduced mechanisms. The trapping of free charge

carriers upto a greater extent eventuates due to an increase in trap state density and hence boosts up the performance of fabricated photomemristive device [78,79].

There are two main mechanisms responsible for the rise in  $I_{on}/I_{off}$  values with external light irradiance. The first one is based on the conductive filament mechanism based on the redox reaction of conducting Ag filament and the second is based on the photogenerated charge carriers in photosensitive materials. These mechanisms work in

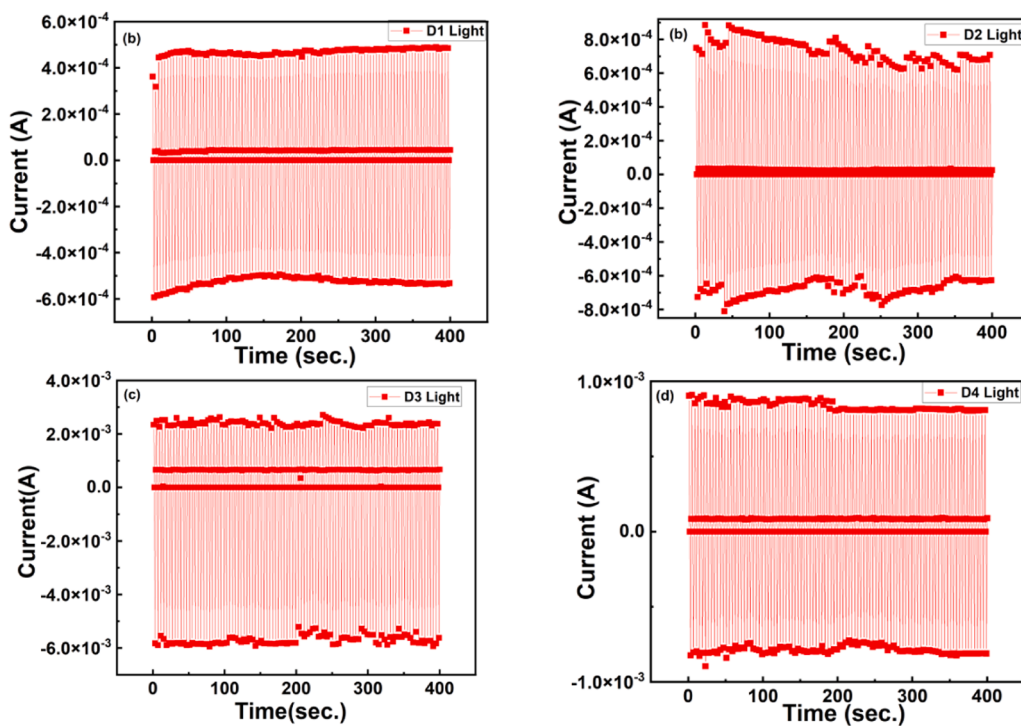


Fig. 31. WRER cycles for (a) Ag/D1/FTO (b) Ag/D2/FTO (c) Ag/D3/FTO and (d) Ag/D4/FTO device in light.

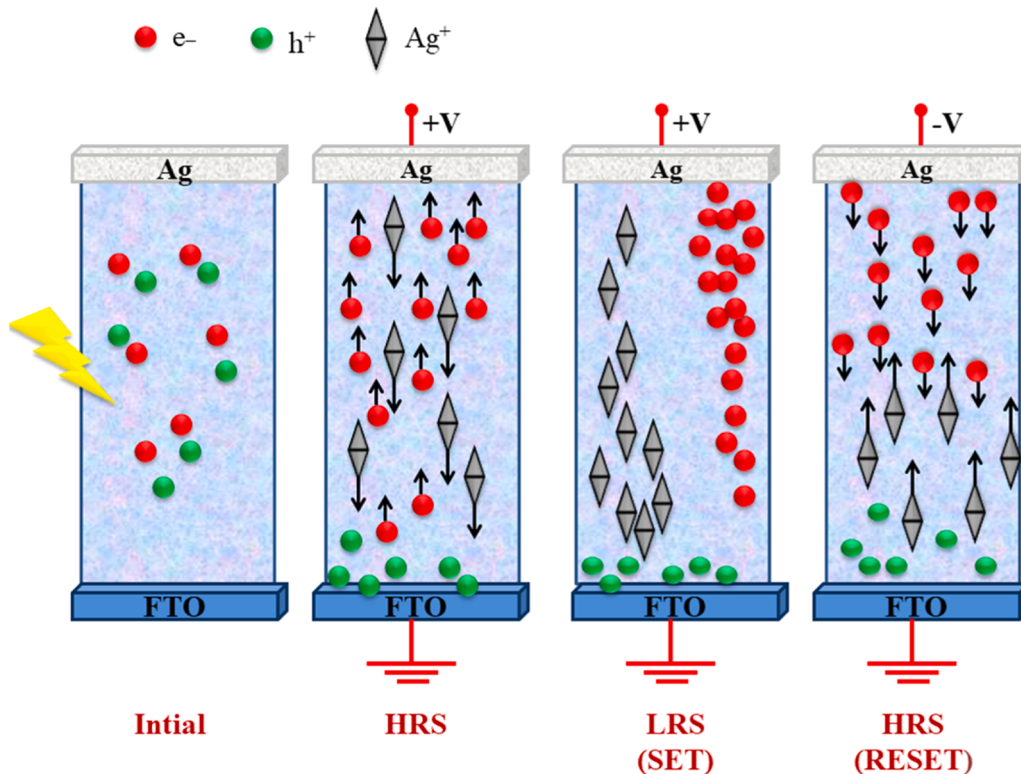


Fig. 32. Schematic of mechanism depicting the influence of incident external light on the hysteresis of synthesized nanocomposites.

association in our case as depicted by Fig. 32 [80]. The incident white light excites the photogenerated charge carriers (e-h pair) within photosensitive MoS<sub>2</sub> when incident photon energy becomes greater than the band gap energy of MoS<sub>2</sub>. These generated charge carriers move towards their respective electrodes under the influence of externally

applied voltage bias. The holes move towards the FTO and electrons move towards the Ag electrode and enhance the oxidation of Ag as Ag<sup>+</sup>. Due to this the formation of conductive filament becomes rapid and easier. The conductivity of the device got enhanced and results in the upgraded performance of the photomemristive device. On the other

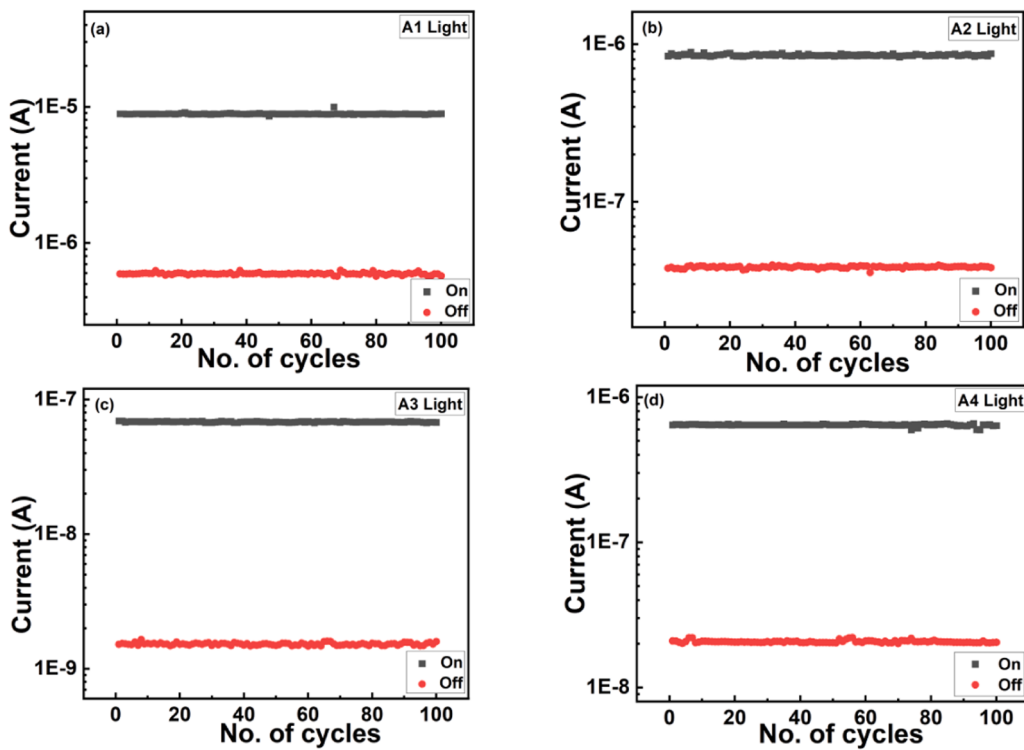


Fig. 33. Endurance characteristics for (a) Ag/A1/FTO (b) Ag/A2/FTO (c) Ag/A3/FTO and (d) Ag/A4/FTO device in Light.

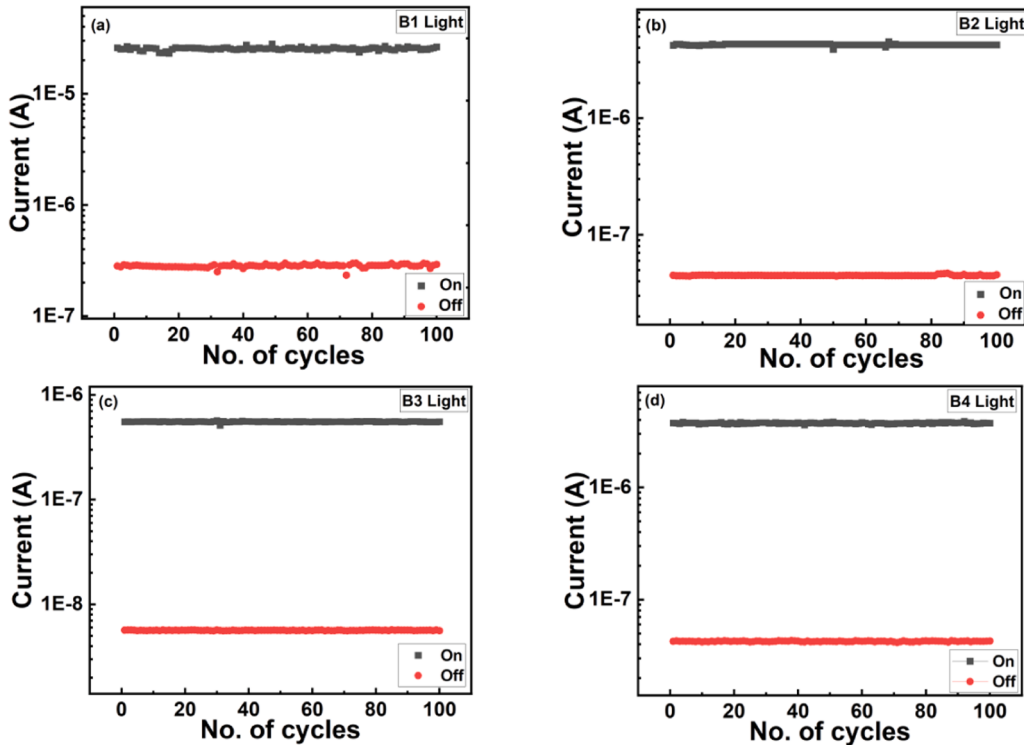


Fig. 34. Endurance characteristics for (a) Ag/B1/FTO (b) Ag/B2/FTO (c) Ag/B3/FTO and (d) Ag/B4/FTO device in Light.

hand, the number of charge carriers increases due to the photo generation of charge carriers resulting in current enhancement. These charge carriers are trapped by defect states on their path toward the respective electrodes due to which there is an enhancement in the  $I_{on}/I_{off}$  values [81]. Similar behavior has been reported in the literature by Chen et al.

[82].

Although there is an increase in  $I_{on}/I_{off}$  value with light but percentage increase is not uniform for all the synthesized samples. From Table 3 we have observed that the percentage increase is high as the MoS<sub>2</sub> concentration increases (upto 1 wt%) because with an increase in

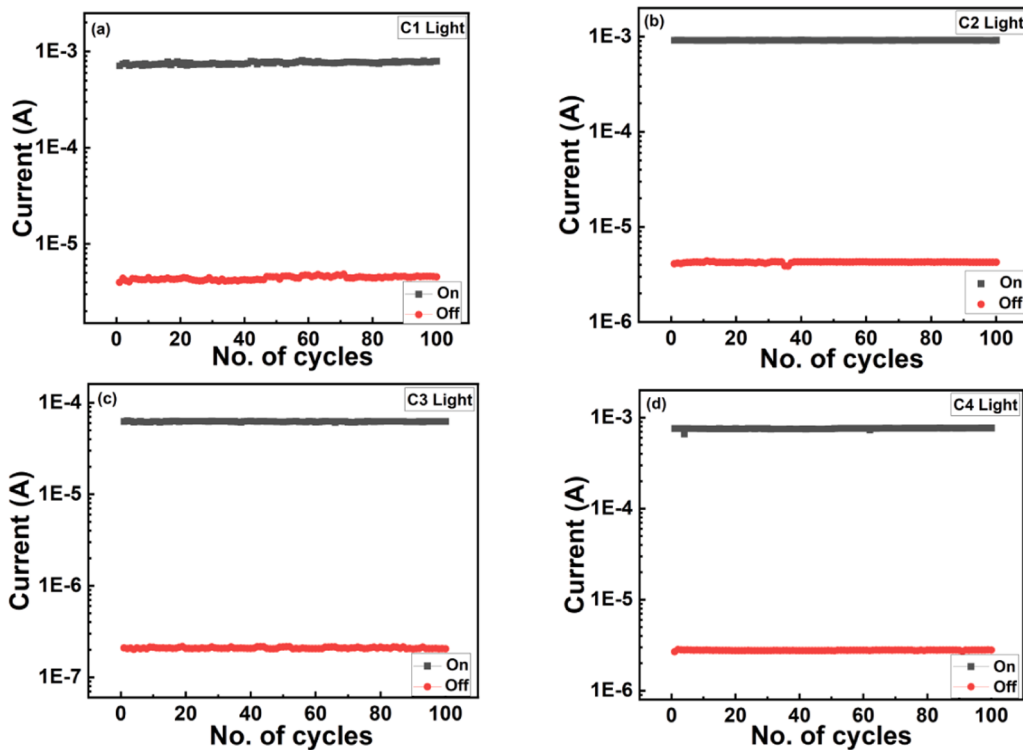


Fig. 35. Endurance characteristics for (a) Ag/C1/FTO (b) Ag/C2/FTO (c) Ag/C3/FTO and (d) Ag/C4/FTO device in Light.

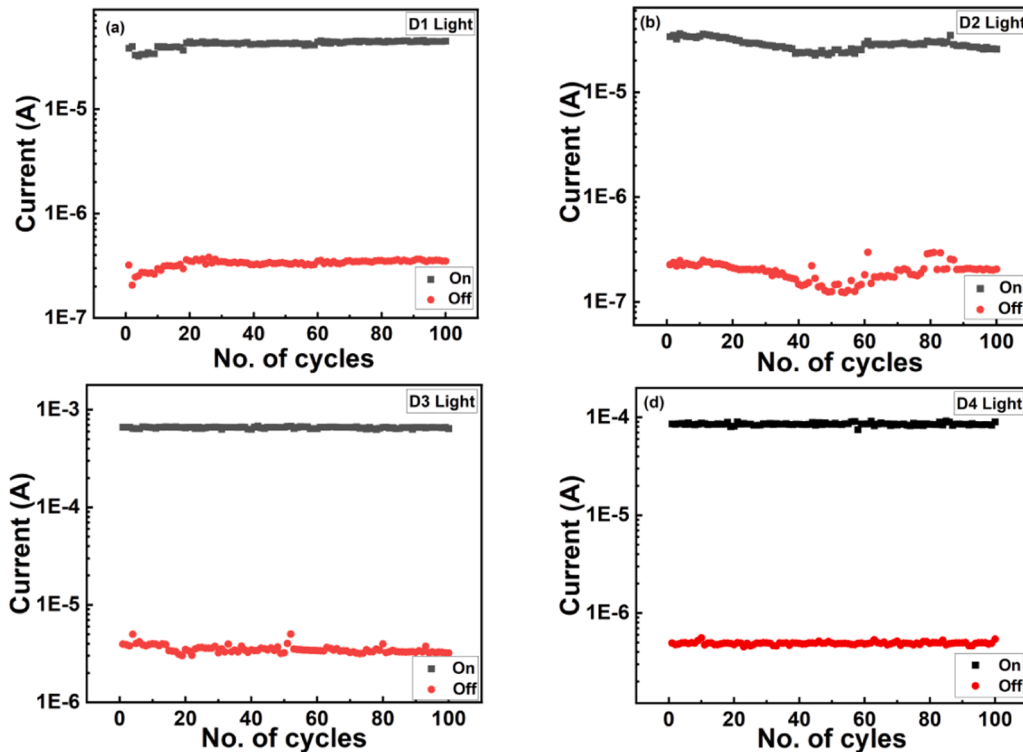


Fig. 36. Endurance characteristics for (a) Ag/D1/FTO (b) Ag/D2/FTO (c) Ag/D3/FTO and (d) Ag/D4/FTO device in Light.

the photosensitive center ( $\text{MoS}_2$  NSs), the number of photogenerated charge carriers increases and more the number of free charge carriers more will be trapping of charge carriers in defect states and more will be the charge storage ratio. With further increase in concentration, upto 1.5 wt% causes the photogeneration of charge carriers in an excessive

amount causing a sudden rise in conductivity and may result in the leakage of stored charge and finally leading to the degraded performance of the device [83].

From Table 3, it has also been observed that for a particular concentration of  $\text{MoS}_2$  within the PVA matrix the %age increase in  $I_{\text{on}}/I_{\text{off}}$

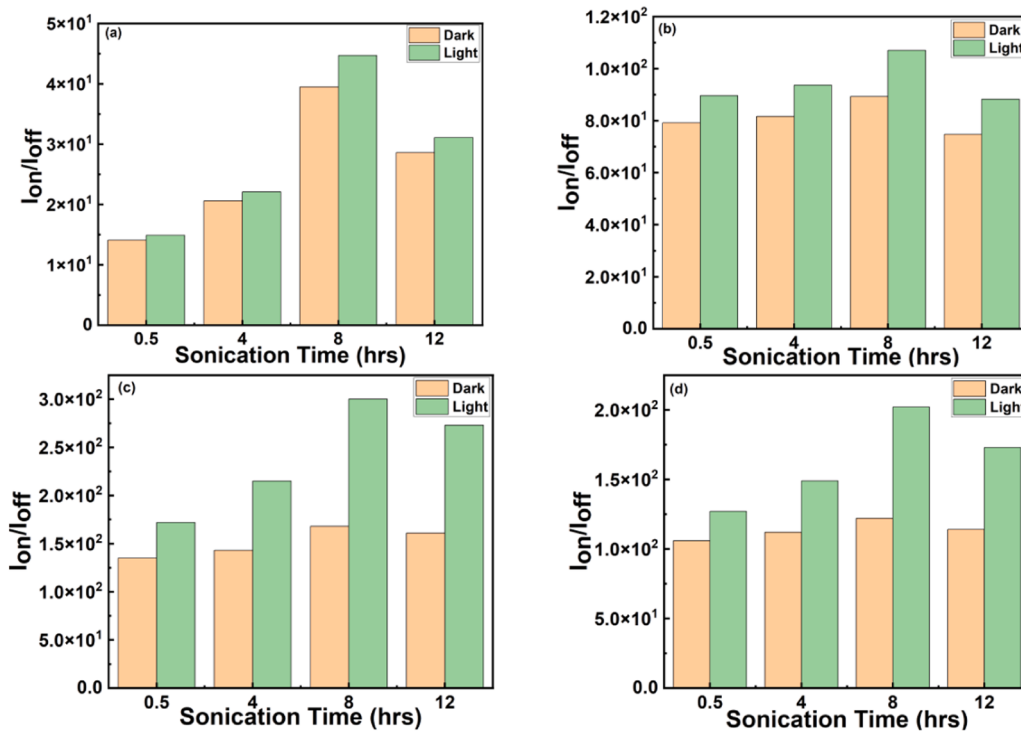


Fig. 37. The variation of  $I_{on}/I_{off}$  values of Ag/MoS<sub>2</sub>-PVA/FTO device with (a) 0.1 wt% (b) 0.5 wt% (c) 1 wt% and (d) 1.5 wt% of MoS<sub>2</sub>/PVA NCPs.

**Table 4**  
Performance comparison of fabricated device with the earlier reported memory devices.

Device architecture	Top Electrode	Method of Deposition	Memory Type	$I_{on}/I_{off}$	Ref.
Ag/MoS <sub>2</sub> -PVA/ FTO	Ag	Dropcasting	Resistive switching	$\sim 3 \times 10^2$	This work
Al/MoS <sub>2</sub> -PVP/rGO/ PET	Al	Dropcasting	Resistive switching	$\sim 10^2$	[84]
Au/HfSe <sub>2</sub> /PMMA/Ti	Au	E-beam evaporation	Resistive switching	$\sim 10^2$	[85]
TiN/O-MoS <sub>2</sub> /TiN	TiN		Resistive switching	$< 10$	[86]
Ag/MoS <sub>2</sub> -PVA/Ag/ PET	Ag	Reverse offset electro hydro dynamic atomization and patterning	Resistive switching	$\sim 1.28 \times 10^2$	[87]
Ti-Au/MoS <sub>2</sub> /Ti-Au	Ti-Au	Atomic layer deposition	Resistive switching	$\sim 10$	[88]
Ag/MoSe <sub>2</sub> /FTO	Ag	Magnetron sputtering	Resistive switching	$\sim 12$	[89]
Ag/MoSe <sub>2</sub> /SiO <sub>2</sub> /Si	Ag	Sputtering	Resistive switching	$\sim 70$	[90]
Ag/MoSe <sub>2</sub> :Se/SiO <sub>2</sub> / Si	Ag	Solution processing	ERSM	$\sim 10^2$	[91]

value with light illumination increases with sonication upto 8 h and decreases with further sonication upto 12 h. In this case, the light illumination and sonication work simultaneously to enhance the performance of the photomemristive device. As explained earlier in this section that with light illumination the trap density increases as well as there is generation of photo-induced charge carriers and with ultrasonication the diffusion length of charge carriers got enhanced which reduces the probability of their recombination. These two factors help in association to boost the  $I_{on}/I_{off}$  value.

Figs. 33–36 display the endurance capabilities over 100 cycles under light illumination for Ag/MoS<sub>2</sub>-PVA/FTO device with 0.1 wt%, 0.5 wt %, 1 wt% and 1.5 wt% of MoS<sub>2</sub>/PVA NCPs (active layer), respectively. The endurance characteristics prove that the stability and sensitivity of the photomemristors got reinforced with light illumination. The optimized concentration of MoS<sub>2</sub>/PVA based photomemristors is 1 wt% MoS<sub>2</sub> in PVA with 8 h of sonication. This device exhibits the  $I_{on}/I_{off}$  ratio of  $\sim 3 \times 10^2$  (from Table 3). Fig. 37 displays the variation of the  $I_{on}/I_{off}$  value of fabricated photomemristors with and without light illumination. The comparison between the present study and previously investigated resistive switching memory is displayed in Table 4.

## 5. Conclusion

In the present work, the MoS<sub>2</sub> NSs and their NCPs with PVA have been successfully synthesized with the help of hydrothermal method and chemical route *In-situ* method, respectively. The XRD spectra reveal the 2H hexagonal phase of MoS<sub>2</sub> NSs. The UV and PL spectroscopy confirms that the synthesized MoS<sub>2</sub> NSs exhibits the characteristics absorption and emission peaks, respectively. FESEM scans confirm the nanoflower type morphology of synthesized NSs. HRTEM scans confirms the crystalline nature of MoS<sub>2</sub> NSs with the help of SAED pattern. The XRD spectra and FESEM scans also confirms the successful incorporation of MoS<sub>2</sub> NSs within the PVA matrix. The FESEM scans of NCPs shows that the ultrasonication enhances the exfoliation of MoS<sub>2</sub> NSs as well as enhances the dispersion of MoS<sub>2</sub> within the polymer matrix. The RAMAN spectra shows that the ultrasonication accelerates the process of exfoliation of NSs and it further confirms that the density of sulfur defects increases with increase in concentration as well as ultrasonication time duration. The cyclic I-V measurements of the fabricated photomemristor show that the performance of the device got augmented by increasing the concentration of MoS<sub>2</sub> NSs within the polymer matrix as well as by varying the ultrasonication time duration. The enhancement in the  $I_{on}/I_{off}$  value of the fabricated device with light illumination suggests that the MoS<sub>2</sub>/PVA is a good candidate for photomemristor application. The

maximum  $I_{on}/I_{off}$  value obtained in present study is  $\sim 3 \times 10^2$ . Hence we can conclude that the MoS<sub>2</sub>/PVA is a good candidate to fabricate stable, reliable, highly efficient and flexible photomemristor.

## CRediT authorship contribution statement

**S.K. Tripathi:** Writing – review & editing, Software, Resources, Project administration, Funding acquisition, Data curation. **Ravneet Kaur:** Writing – review & editing, Methodology, Investigation, Data curation, Conceptualization. **Krishma Anand:** Writing – review & editing, Writing – original draft, Visualization, Software, Methodology, Investigation, Data curation, Conceptualization.

## Declaration of Competing Interest

The authors declare that they have no known competing financial interests or personal relationships that could have appeared to influence the work reported in this paper.

## Acknowledgments

Ms. Krishna Anand is thankful to CSIR for providing financial support.

## Data availability

Data will be made available on request.

## References

- [1] M.E. Pereira, R. Martins, E. Fortunato, P. Barquinha, A. Kiaziadeh, Recent progress in optoelectronic memristors for neuromorphic and in-memory computation, *Neuromorphic Comput. Eng.* 3 (2023) 2002, <https://doi.org/10.1088/2634-4386/acd4e2>.
- [2] R. El Hage, V. Humbert, V. Rouco, G. Sánchez-Santolino, A. Lagarrigue, K. Seurre, S.J. Carreira, A. Sander, J. Charlier, S. Mesoraca, J. Trastoy, J. Briatico, J. Santamaría, J.E. Villegas, Bimodal ionic photomemristor based on a high-temperature oxide superconductor/semiconductor junction, *Nat. Commun.* 14 (2023) 1–10, <https://doi.org/10.1038/s41467-023-38608-0>.
- [3] H. Xu, J. Zhu, Q. Ma, J. Ma, H. Bai, L. Chen, S. Mu, Two-dimensional MoS<sub>2</sub>: Structural properties, synthesis methods, and regulation strategies toward oxygen reduction, *Micromachines* 12 (2021) 1–23, <https://doi.org/10.3390/mi12030240>.
- [4] C.S. Prasanna, V. Shalini V, S. Harish, S.K. Eswaran, H. Ikeda, M. Navaneethan, Solution-processed MoS<sub>2</sub> nanostructures and thermal oxidation on carbon fabric with enhanced thermopower factor for wearable thermoelectric application, *J. Alloy. Compd.* 1002 (2024) 175168, <https://doi.org/10.1016/j.jallcom.2024.175168>.
- [5] S. Lee, Y.K. Kim, J.Y. Hong, J. Jang, Electro-response of MoS<sub>2</sub> nanosheets-based smart fluid with tailorable electrical conductivity, *ACS Appl. Mater. Interfaces* 8 (2016) 24221–24229, <https://doi.org/10.1021/acsami.6b07887>.
- [6] G. Tang, Y. Chen, J. Yin, S. Shen, K. Cai, Preparation, characterization and properties of MoS<sub>2</sub> nanosheets via a microwave-assisted wet-chemical route, *Ceram. Int.* 44 (2018) 5336–5340, <https://doi.org/10.1016/j.ceramint.2017.12.152>.
- [7] V. Gunasekaran, M.K. Devaraju, S. Yuvaraj, V.J.Y. Surya, V. Singh, K. Karthikeyan, S.J. Kim, Electrical transport properties of two-dimensional MoS<sub>2</sub> nanosheets synthesized by novel method, *Mater. Sci. Semicond. Process.* 66 (2017) 81–86, <https://doi.org/10.1016/j.mssp.2017.04.011>.
- [8] J.H. Kim, T.H. Kim, H. Lee, Y.R. Park, W. Choi, C.J. Lee, Thickness-dependent electron mobility of single and few-layer MoS<sub>2</sub> thin-film transistors, *AIP Adv.* 6 (2016) 2–7, <https://doi.org/10.1063/1.4953809>.
- [9] T. Dutta, N. Yadav, Y. Wu, G.J. Cheng, X. Liang, S. Ramakrishna, A. Sbai, R. Gupta, A. Mondal, Z. Hongyu, A. Yadav, Electronic properties of 2D materials and their junctions, *Nano Mater. Sci.* 6 (2024) 1–23, <https://doi.org/10.1016/j.namoms.2023.05.003>.
- [10] L. Liu, Y. Wang, W. Chen, S. Ren, J. Guo, X. Kang, X. Zhao, Robust resistive switching in MoS<sub>2</sub>-based memristor with Ti top electrode, *Appl. Surf. Sci.* 605 (2022) 154698, <https://doi.org/10.1016/j.apsusc.2022.154698>.
- [11] R. Yang, L. Mei, Q. Zhang, Y. Fan, H.S. Shin, D. Voiry, Z. Zeng, High-yield production of mono- or few-layer transition metal dichalcogenide nanosheets by an electrochemical lithium ion intercalation-based exfoliation method, *Nat. Protoc.* 17 (2022) 358–377, <https://doi.org/10.1038/s41596-021-00643-w>.
- [12] P. Dong, J. Jian, H. Feng, M. Geng, B. Dang, Q. Gao, J. Xu, M. Zhu, X. Liu, Multi-level storage characteristics of MoSe<sub>2</sub> resistive random access memory, *J. Phys. Conf. Ser.* 2731 (2024) 012032, <https://doi.org/10.1088/1742-6596/2731/1/012032>.
- [13] S. Saini, A. Dwivedi, A. Lodhi, A. Khandelwal, S.P. Tiwari, Flexible Forming Free Resistive Memory Device with 2D Material MoSe<sub>2</sub> as Switching Layer, 7th IEEE Electron Devices Technol. Manuf. Conf. Strengthen Glob. Semicond. Res. Collab. After Covid-19 Pandemic, EDTM 2023 1, 2023, pp. 1–3. doi: [10.1109/EDTM55494.20.23.10103025](https://doi.org/10.1109/EDTM55494.20.23.10103025).
- [14] Z.W. Dlamini, S. Vallabhapurapu, A. Srinivasan, S. Wu, V.S. Vallabhapurapu, Resistive Switching in Polyvinylpyrrolidone/Molybdenum Disulfide Composite-Based Memory Devices, *Acta Phys. Pol. A* 141 (2022) 439–444, <https://doi.org/10.12693/APhysPolA, 141.439>.
- [15] R. Deb, P. Pathak, S.R. Mohapatra, U. Das, Polarity independent resistive switching in MoS<sub>2</sub>nanosheets and PEO-based nanocomposite films, *Jpn. J. Appl. Phys.* 61 (SM) (2022) 1004, <https://doi.org/10.35848/1347-4065/ac6053>.
- [16] M.M. Rehman, G.U. Siddiqui, J.Z. Gul, S.W. Kim, J.H. Lim, K.H. Choi, Resistive Switching in All-Printed, Flexible and Hybrid MoS<sub>2</sub>-PVA Nanocomposite based Memristive Device Fabricated by Reverse Offset, *Sci. Rep.* 6 (2016) 1–10, <https://doi.org/10.1038/srep36195>.
- [17] T.S. Soliman, S.A. Vshivkov, Effect of Fe nanoparticles on the structure and optical properties of polyvinyl alcohol nanocomposite films, *J. Non Cryst. Solids* 519 (2019) 119452, <https://doi.org/10.1016/j.jnoncrysol.2019.05.028>.
- [18] R. Jyoti, S. Kaur, J. Singh, S.K. Sharma, Tripathi, Effect of TiO<sub>2</sub> concentration on the non-volatile memory behavior of TiO<sub>2</sub>-PVA polymer nanocomposites, *J. Electron. Mater.* 48 (2019) 5995–6002, <https://doi.org/10.1007/s11664-019-07327-y>.
- [19] H. Wang, X. Xu, A. Neville, Facile synthesis of vacancy-induced 2H-MoS<sub>2</sub>nanosheets and defect investigation for supercapacitor application, *RSC Adv.* 11 (2021) 26273–26283, <https://doi.org/10.1039/dra04902>.
- [20] K. Anand, R. Kaur, A. Arora, S.K. Tripathi, Tuning of linear and non-linear optical properties of MoS<sub>2</sub>/PVA nanocomposites via ultrasonication, *Opt. Mater.* 137 (2023) 113523, <https://doi.org/10.1016/j.optmat.2023.113523>.
- [21] C.P. Veeramalai, F. Li, Y. Liu, Z. Xu, T. Guo, T.W. Kim, Enhanced field emission properties of molybdenum disulphide few layer nanosheets synthesized by hydrothermal method, *Appl. Surf. Sci.* 389 (2016) 1017–1022, <https://doi.org/10.1016/j.apsusc.2016.08.031>.
- [22] Y. Zhang, L. Zuo, Y. Huang, L. Zhang, F. Lai, W. Fan, T. Liu, In-situ growth of few-layered MoS<sub>2</sub> nanosheets on highly porous carbon aerogel as advanced electrocatalysts for hydrogen evolution reaction, *ACS Sustain. Chem. Eng.* 3 (2015) 3140–3148, <https://doi.org/10.1021/acssuschemeng.5b00700>.
- [23] L. Yang, X. Cui, J. Zhang, K. Wang, M. Shen, S. Zeng, S.A. Dayeh, L. Feng, B. Xiang, Lattice strain effects on the optical properties of MoS<sub>2</sub> nanosheets, *Sci. Rep.* 4 (2014) 1–7, <https://doi.org/10.1038/srep05649>.
- [24] D. Sahoo, S.P. Behera, J. Shakya, B. Kaviraj, Cost-effective synthesis of 2D molybdenum disulfide (MoS<sub>2</sub>) nanocrystals: An exploration of the influence on cellular uptake, cytotoxicity, and bio-imaging, *PLoS One* 17 (2022) e0260955, <https://doi.org/10.1371/journal.pone.0260955>.
- [25] S.K. Tripathi, R. Kaur, Jyoti, Investigation of non-linear optical properties of CdS/PS polymer nanocomposite synthesized by chemical route, *Opt. Commun.* 352 (2015) 55–62, <https://doi.org/10.1016/j.optcom.2015.04.042>.
- [26] S.J. Adilla, E. Nurfani, R. Kurniawan, C.D. Satrya, Y. Darma, Structural and optical properties analysis of MoS<sub>2</sub> nanoflakes on quartz substrate as prepared by mechanical exfoliation, *J. Phys. Conf. Ser.* 877 (2017) 012036, <https://doi.org/10.1088/1742-6596/877/1/012036>.
- [27] R. Kaur, K.P. Singh, S.K. Tripathi, Preparation and incorporation of NiSe@MoSe<sub>2</sub> nano arrays in PVA matrix for resistive switching memory, *J. Alloy. Compd.* 925 (2022) 166607, <https://doi.org/10.1016/j.jallcom.2022.166607>.
- [28] A. Tools, D. Help, E. Pmc, Hydrogen evolution reaction from bare and surface-functionalized few-layered MoS<sub>2</sub> nanosheets in acidic and alkaline electrolytes, *Mater. Today Chem.* 14 (2019) 1–21, <https://doi.org/10.1016/j.mtchem.2019.100207>.
- [29] A. Arora, K. Sharma, S.K. Tripathi, Influence of precursors on hydrothermal synthesis and electronic properties of molybdenum diselenide, *Appl. Phys. A Mater. Sci. Process.* 129 (2023) 654, <https://doi.org/10.1007/s00339-023-06897-3>.
- [30] N. Manyani, P. Siwatch, S. Rana, K. Sharma, S.K. Tripathi, Study of electrochemical behaviour of binder-free nickel metal-organic framework derived by benzene-1,3,5-tricarboxylic acid for supercapacitor electrode, *Mater. Res. Bull.* 165 (2023) 112320, <https://doi.org/10.1016/j.materresbull.2023.112320>.
- [31] P. Berwal, S. Rani, S. Sihag, P. Singh, R. Dahiya, A. Kumar, A. Sanger, A.K. Mishra, V. Kumar, Hydrothermal synthesis of MoS<sub>2</sub> with tunable band gap for future nano-electronic devices, *Inorg. Chem. Commun.* 159 (2024) 111833, <https://doi.org/10.1016/j.inoche.2023.111833>.
- [32] G. Deokar, D. Vignaud, R. Arenal, P. Louette, J.F. Colomer, Synthesis and characterization of MoS<sub>2</sub> nanosheets, *Nanotechnology* 27 (2016) 075604, <https://doi.org/10.1088/0957-4484/27/7/075604>.
- [33] T.T. Xuan, L.N. Long, T. Van Khai, Effect of reaction temperature and reaction time on the structure and properties of MoS<sub>2</sub> synthesized by hydrothermal method, *Vietnam J. Chem.* 58 (2020) 92–100, <https://doi.org/10.1002/vjch.2019000144>.
- [34] S. Mukherjee, R. Maiti, A. Midya, S. Das, S.K. Ray, Tunable direct bandgap optical transitions in MoS<sub>2</sub> nanocrystals for photonic devices, *ACS Photonics* 2 (2015) 760–768, <https://doi.org/10.1021/acsphtronics.5b00111>.
- [35] D. Pierucci, H. Henck, C.H. Naylor, H. Sediri, E. Lhuillier, A. Balan, J.E. Rault, Y. J. Dappe, F. Bertran, P. Le Fèvre, A.T.C. Johnson, A. Ouerghi, Large area molybdenum disulphide epitaxial graphene vertical Van der Waals heterostructures, *Sci. Rep.* 6 (2016) 26656, <https://doi.org/10.1038/srep26656>.
- [36] D. Sahoo, B. Kumar, J. Sinha, S. Ghosh, S.S. Roy, B. Kaviraj, Cost effective liquid phase exfoliation of MoS<sub>2</sub> nanosheets and photocatalytic activity for wastewater

- treatment enforced by visible light, *Sci. Rep.* 10 (2020) 1–12, <https://doi.org/10.1038/s41598-020-67683-2>.
- [37] J. Wan, R. Wang, L. Liu, J. Fan, E. Liu, X. Gao, F. Fu, A novel approach for high-yield solid few-layer MoS<sub>2</sub> nanosheets with effective photocatalytic hydrogen evolution, *Int. J. Hydrogen Energy* 44 (2019) 16639–16647, <https://doi.org/10.1016/j.ijhydene.2019.04.150>.
- [38] D. Timmerman, T. Gregorkiewicz, On the power-dependent spectral shift of photoluminescence from ensembles of silicon nanocrystals, *Nanoscale Res. Lett.* 7 (2012) 1–6, <https://doi.org/10.1186/1556-276X-7-389>.
- [39] G. Kamada, G. Venugopal, M. Kotsugi, T. Ohkochi, M. Suemitsu, H. Fukidome, Element- and Site-Specific Many-Body Interactions in Few-Layer MoS<sub>2</sub> During X-Ray Absorption Processes, *Phys. Status Solidi Appl. Mater. Sci.* 216 (2019) 1–7, <https://doi.org/10.1002/pssa.201800539>.
- [40] S. Santhosh, A.A. Madhavan, A review on the structure, properties and characterization of 2D Molybdenum Disulfide, 2019 *Adv. Sci. Eng. Technol. Int. Conf. ASET 2019* (2019) 1–5, <https://doi.org/10.1109/ICASET.2019.8714360>.
- [41] S. Tajik, Z. Dourandish, F.G. Nejad, A. Aghaei Afshar, H. Beitolahli, Voltammetric determination of isoniazid in the presence of acetaminophen utilizing MoS<sub>2</sub>-nanosheet-modified screen-printed electrode, *Micromachines* 13 (2022) 369, <https://doi.org/10.33.90/mi13030369>.
- [42] M. Moradi-Bieravand, S. Farhadi, A. Zabardasti, F. Mahmoudi, Construction of magnetic MoS<sub>2</sub>/NiFe<sub>2</sub>O<sub>4</sub>/MIL-101(Fe) hybrid nanostructures for separation of dyes and antibiotics from aqueous media, *RSC Adv.* 14 (2024) 11037–11056, <https://doi.org/10.1039/d4ra00505h>.
- [43] A. Gopalakrishnan, S.P. Singh, S. Badhulika, Reusable, few-layered-MoS<sub>2</sub> nanosheets/graphene hybrid on cellulose paper for superior adsorption of methylene blue dye, *New J. Chem.* 44 (2020) 5489–5500, <https://doi.org/10.1039/d0nj00246a>.
- [44] N. Kumar, P. Sirohi, Y. Sharma, D. Singh, K.K. Dey, R. Kumar, H. Borkar, J. Gangwar, Probing on crystallographic structural and surface morphology of hydrothermally synthesized MoS<sub>2</sub> nanoflowers consisting of nanosheets, *Appl. Surf. Sci. Adv.* 6 (2021) 100167, <https://doi.org/10.1016/j.apsadv.2021.100167>.
- [45] R. Khatri, N.K. Puri, Electrochemical study of hydrothermally synthesised reduced MoS<sub>2</sub> layered nanosheets, *Vacuum* 175 (2020) 109250, <https://doi.org/10.1016/j.vacuum.2020.109250>.
- [46] A. Raza, M. Ikram, M. Aqeel, M. Imran, A. Ul-Hamid, K.N. Riaz, S. Ali, Enhanced industrial dye degradation using Co doped in chemically exfoliated MoS<sub>2</sub> nanosheets, *Appl. Nanosci.* 10 (2020) 1535–1544, <https://doi.org/10.1007/s13204-019-01239-3>.
- [47] H. Wang, P. Fang, Z. Chen, S. Wang, Synthesis and characterization of CdS/PVA nanocomposite films, *Appl. Surf. Sci.* 253 (2007) 8495–8499, <https://doi.org/10.1016/j.apsusc.2007.04.020>.
- [48] C.M. Tang, Y.H. Tian, S.H. Hsu, Poly(vinyl alcohol) nanocomposites reinforced with bamboo charcoal nanoparticles: mineralization behavior and characterization, *Materials* 8 (2015) 4895–4911, <https://doi.org/10.3390/ma8084895>.
- [49] S. Huo, P. Song, B. Yu, S. Ran, V.S. Chevali, L. Liu, Z. Fang, H. Wang, Phosphorus-containing flame retardant epoxy thermosets: Recent advances and future perspectives, *Prog. Polym. Sci.* 114 (2021) 101366, <https://doi.org/10.1016/j.progpolymsci.2021.101366>.
- [50] M. Vasudevan, M.J.Y. Tai, V. Perumal, S.C.B. Gopinath, S.S. Murthe, M. Ovinis, N. M. Mohamed, N. Joshi, Cellulose acetate-MoS<sub>2</sub> nanopetal hybrid: a highly sensitive and selective electrochemical aptasensor of Troponin I for the early diagnosis of Acute Myocardial Infarction, *J. Taiwan Inst. Chem. Eng.* 118 (2021) 245–253, <https://doi.org/10.1016/j.jitec.2021.01.016>.
- [51] N.S. Taghavi, R. Afzalzadeh, The effect of sonication parameters on the thickness of the produced MoS<sub>2</sub> nano-flakes, *Arch. Acoust.* 46 (2021) 31–40, <https://doi.org/10.24425/aoa.2021.136558>.
- [52] A. Ratan, S. Kunchakara, M. Dutt, A. Tripathi, V. Singh, Enhanced electrical properties of few layers MoS<sub>2</sub>-PVA nanocomposite film via homogeneous dispersion and annealing effect induced by 80 MeV Carbon+ swift heavy ion irradiation, *Mater. Sci. Semicond. Process.* 108 (2020) 104877, <https://doi.org/10.1016/j.mss.2019.104877>.
- [53] L. Jia, J. Wu, T. Yang, B. Jia, D.J. Moss, Large third-order optical Kerr nonlinearity in nanometer-Thick PdSe<sub>2</sub> 2D dichalcogenide films: implications for nonlinear photonic devices, *ACS Appl. Nano Mater.* 3 (2020) 6876–6883, <https://doi.org/10.1021/acsnano.0c01239>.
- [54] K.S. Somvanshi, P.C. Gope, Effect of ultrasonication and fiber treatment on mechanical and thermal properties of polyvinyl alcohol/cellulose fiber nano-biocomposite film, *Polym. Compos.* 42 (2021) 5310–5322, <https://doi.org/10.1002/poc.26225>.
- [55] S. Cortijo-campos, C. Prieto, A. De Andrés, Size effects in single- and few-layer MoS<sub>2</sub> nanoflakes: impact on raman phonons and photoluminescence, *Nanomatials* 12 (2022) 1–17, <https://doi.org/10.3390/nano12081330>.
- [56] W. Shi, M.L. Lin, Q.H. Tan, X.F. Qiao, J. Zhang, P.H. Tan, Raman and photoluminescence spectra of two-dimensional nanocrystallites of monolayer WS<sub>2</sub> and WSe<sub>2</sub>, *2D Mater.* 3 (2016) 1–10, <https://doi.org/10.1088/2053-1583/3/2/025016>.
- [57] R. Kaur, S.K. Tripathi, Dopant dependent electrical switching characteristics of a CdSe Poly(vinyl-pyrrolidone) nanocomposite, *Org. Electron.* 61 (2018) 235–241, <https://doi.org/10.1016/j.orgel.2018.05.060>.
- [58] R. Kaur, J. Singh, S.K. Tripathi, Incorporation of inorganic nanoparticles into an organic polymer matrix for data storage application, *Curr. Appl. Phys.* 17 (2017) 756–762, <https://doi.org/10.1016/j.cap.2017.02.011>.
- [59] M.K. Rahmani, S.A. Khan, H. Kim, M.U. Khan, J. Kim, J. Bae, M.H. Kang, Demonstration of high-stable bipolar resistive switching and bio-inspired synaptic characteristics using PEDOT:PSS-based memristor devices, *Org. Electron.* 114 (2023) 106730, <https://doi.org/10.1016/j.orgel.2022.106730>.
- [60] M.A.A. Khushaini, N.H. Azeman, A.G. Ismail, C.H. Teh, M.M. Salleh, A.A.A. Bakar, T.H.T.A. Aziz, A.R.M. Zain, High stability resistive switching mechanism of a screen-printed electrode based on BOBZBT<sub>2</sub> organic pentamer for creatinine detection, *Sci. Rep.* 11 (2021) 1–11, <https://doi.org/10.1038/s41598-021-03046-9>.
- [61] H. Wang, L. Hu, W. Han, Resistive switching behavior, mechanism and synaptic characteristics in TiO<sub>2</sub> nanosheets grown on Ti plate by hydrothermal method, *J. Alloy. Compd.* 854 (2021) 157200, <https://doi.org/10.1016/j.jallcom.2020.157200>.
- [62] X. Lei, X. Zhu, H. Wang, Y. Dai, H. Zhang, C. Zhai, S. Wang, J. Yan, W. Zhao, Nonvolatile and volatile resistive switching characteristics in MoS<sub>2</sub> thin film for RRAM application, *J. Alloy. Compd.* 969 (2023) 172443, <https://doi.org/10.1016/j.jallcom.2023.172443>.
- [63] F. Zahoor, F.A. Hussin, U.B. Isyaku, S. Gupta, F.A. Khanday, A. Chattopadhyay, H. Abbas, Resistive random access memory: introduction to device mechanism, materials and application to neuromorphic computing, *Springer US* 18 (2023) 36, <https://doi.org/10.1186/s11671-023-03775-y>.
- [64] Z. Xu, Y. Li, Y. Xia, C. Shi, S. Chen, C. Ma, C. Zhang, Y. Li, Organic frameworks memristor: an emerging candidate for data storage, artificial synapse, and neuromorphic device, *Adv. Funct. Mater.* 34 (2024) 1–22, <https://doi.org/10.1002/adfm.202312658>.
- [65] K. John, U., S. Mathew, Z-scan investigations on the third order nonlinear optical properties of flower-like CdZnTe microstructures, *Appl. Phys. A Mater. Sci. Process.* 128 (2022) 1–11, <https://doi.org/10.1007/s00339-022-05395-2>.
- [66] J.J.L. Hmar, Flexible resistive switching bistable memory devices using ZnO nanoparticles embedded in polyvinyl alcohol (PVA) matrix and poly(3,4-ethylenedioxythiophene) polystyrene sulfonate (PEDOT:PSS), *RSC Adv.* 8 (2018) 20423–20433, <https://doi.org/10.1039/c8ra04582h>.
- [67] R.A. Farade, N.I.A. Wahab, D.E.A. Mansour, N.B. Azis, J.B. Jasni, V. Veerasamy, M. Thirumeni, A.X.R. Irudayraj, A.S. Murthy, Investigation of the effect of sonication time on dispersion stability, dielectric properties, and heat transfer of graphene based green nanofluids, *IEEE Access* 9 (2021) 50607–50623, <https://doi.org/10.1109/ACCESS.2021.306928>.
- [68] R.M. Burbelo, O.Y. Olikh, M.K. Hinders, The dynamic ultrasound influence on the diffusion and drift of the charge carriers in silicon p-n structures, *Mater. Res. Soc. Symp. Proc.* 994 (2007) 269–274, <https://doi.org/10.1557/proc-0994-103-11>.
- [69] O.Y. Olikh, I.V. Ostrovskii, Ultrasound-stimulated increase in the electron diffusion length in p-Si crystals, *Phys. Solid State* 44 (2002) 1249–1253, <https://doi.org/10.1134/1.1494617>.
- [70] M.A. Ahmed, A.A. Mohamed, Advances in ultrasound-assisted synthesis of photocatalysts and sonophotocatalytic processes: a review, *IScience* 27 (2024) 108583, <https://doi.org/10.1016/j.isci.2023.108583>.
- [71] Y. Wang, M.R. Ahmadian-Yazdi, Y. Ni, Y. Jiang, M. Eslamian, Z. Jin, Q. Chen, Boosted charge-carrier transport in triple-cation perovskites by ultrasonic vibration post treatment, *Adv. Electron. Mater.* 8 (2022) 1–9, <https://doi.org/10.1002/aelm.202101286>.
- [72] L. Wang, Y. Wang, D. Wen, Switching-enhanced RRAM for reliable synaptic simulation and multilevel data storage, *J. Alloy. Compd.* 892 (2022) 162180, <https://doi.org/10.1016/j.jallcom.2021.162180>.
- [73] Z.Q. Wang, H.Y. Xu, L. Zhang, X.H. Li, J.G. Ma, X.T. Zhang, Y.C. Liu, Performance improvement of resistive switching memory achieved by enhancing local-electric-field near electromigrated Ag-nanoclusters, *Nanoscale* 5 (2013) 4490–4494, <https://doi.org/10.1039/c3nr33692a>.
- [74] D. Jana, S. Chakrabarti, S.Z. Rahaman, S. Maikap, Resistive and new optical switching memory characteristics using thermally grown Ge<sub>0.2</sub>Se<sub>0.8</sub> film in Cu/GeSe<sub>x</sub>/W structure, *Nanoscale Res. Lett.* 10 (2015) 1–8, <https://doi.org/10.1186/s11671-015-1090-1>.
- [75] D. Jana, S. Chakrabarti, S.Z. Rahaman, S. Maikap, Resistive and new optical switching memory characteristics using thermally grown Ge<sub>0.2</sub>Se<sub>0.8</sub> film in Cu/GeSe<sub>x</sub>/W structure, *Nanoscale Res. Lett.* 10 (2015) 1–8, <https://doi.org/10.1186/s11671-015-1090-1>.
- [76] D. Kufer, G. Konstantatos, Highly sensitive, encapsulated MoS<sub>2</sub> Photodetector with Gate Controllable Gain and Speed, *Nano Lett.* 15 (2015) 7307–7313, <https://doi.org/10.1021/acs.nanolett.5b02559>.
- [77] W. Wang, G.N. Panin, X. Fu, L. Zhang, P. Ilanchezhian, V.O. Pelenovich, D. Fu, T. W. Kang, MoS<sub>2</sub> memristor with photoresistive switching, *Sci. Rep.* 6 (2016) 1–11, <https://doi.org/10.1038/srep31224>.
- [78] R.A. Street, Y. Yang, B.C. Thompson, I. McCulloch, Capacitance spectroscopy of light induced trap states in organic solar cells, *J. Phys. Chem. C* 120 (2016) 22169–22178, <https://doi.org/10.1021/acs.jpcc.6b06561>.
- [79] S. Paramanik, A.J. Pal, Combining negative photoconductivity and resistive switching towards in-memory logic operations, *Nanoscale* 15 (2023) 5001–5010, <https://doi.org/10.1039/d3nr00278k>.
- [80] W. Wang, S. Gao, Y. Wang, Y. Li, W. Yue, H. Niu, F. Yin, Y. Guo, G. Shen, Advances in emerging photonic memristive and memristive-like devices, *Adv. Sci.* 9 (2022) 1–39, <https://doi.org/10.1002/advs.202105577>.
- [81] Z. Sheykifar, S.M. Mohseni, Highly light-tunable memristors in solution-processed 2D materials/metal composites, *Sci. Rep.* 12 (2022) 1–12, <https://doi.org/10.1038/s41598-022-23404-5>.
- [82] Z. Chen, Y. Yu, L. Jin, Y. Li, Q. Li, T. Li, J. Li, H. Zhao, Y. Zhang, H. Dai, J. Yao, Broadband photoelectric tunable quantum dot based resistive random access memory, *J. Mater. Chem. C* 8 (2020) 2178–2185, <https://doi.org/10.1039/c9tc06230k>.

- [83] A. Kalateh, A. Jalali, M.J. Kamali Ashtiani, M. Mohammadimasoudi, H. Bastami, M. Mohseni, Resistive switching transparent SnO<sub>2</sub> thin film sensitive to light and humidity, *Sci. Rep.* 13 (2023) 1–11, <https://doi.org/10.1038/s41598-023-45790-0>.
- [84] Z. Zhou, F. Yang, S. Wang, L. Wang, X. Wang, C. Wang, Y. Xie, Q. Liu, Emerging of two-dimensional materials in novel memristor, *Front. Phys.* 17 (2022) 1–14, <https://doi.org/10.1007/s11467-021-1114-5>.
- [85] S. Li, M.E. Pam, Y. Li, L. Chen, Y.C. Chien, X. Fong, D. Chi, K.W. Ang, Wafer-Scale 2D hafnium diselenide based memristor crossbar array for energy-efficient neural network hardware, *Adv. Mater.* 34 (2022) 1–12, <https://doi.org/10.1002/adma.20210.3376>.
- [86] X. Xiong, F. Wu, Y. Ouyang, Y. Liu, Z. Wang, H. Tian, M. Dong, Oxygen incorporated MoS<sub>2</sub> for rectification-mediated resistive switching and artificial neural network, *Adv. Funct. Mater.* 34 (2024) 1–8, <https://doi.org/10.1002/adfm.202213348>.
- [87] M. Sloma, 3D printed electronics with nanomaterials, *Nanoscale* 15 (2023) 5623–5648, <https://doi.org/10.1039/d2nr06771d>.
- [88] Y. Zhao, Y. Jin, X. Wang, J. Zhao, S. Wu, M. Li, J. Wang, S. Fan, Q. Li, A high linearity and energy-efficient artificial synaptic device based on scalable synthesized MoS<sub>2</sub>, *J. Mater. Chem. C* 11 (2023) 5616–5624, <https://doi.org/10.1039/d3tc00438d>.
- [89] W. Zhang, M. Gao, X. Lei, C. Zhai, Z. Zhang, Novel memristor with Au/SnSe/ITO structure: first fabrication via a hydrothermal and sputtering approach, *J. Alloy. Compd.* 994 (2024) 174742, <https://doi.org/10.1016/j.jallcom.2024.174742>.
- [90] A. Rani, A.C. Khot, I.G. Jang, T.G. Kim, Heterostructure carbon-packed MoSSe nanospheres for flexible ReRAM and synapse devices, *Carbon N. Y.* 189 (2022) 104–112, <https://doi.org/10.1016/j.carbon.2021.12.057>.
- [91] M. Khan, H.M. Mutee Ur Rehman, R. Tehreem, M. Saqib, M.M. Rehman, W.Y. Kim, All-printed flexible memristor with metal–non-metal-doped TiO<sub>2</sub> nanoparticle thin films, *Nanomaterials* 12 (2022) 1–12, <https://doi.org/10.3390/nano12132289>.